Geophysical Journal International

Geophys. J. Int. (2022) **228,** 366–386
Advance Access publication 2021 August 6
GJI Seismology

https://doi.org/10.1093/gji/ggab347

Sensitivity of SK(K)S and ScS phases to heterogeneous anisotropy in the lowermost mantle from global wavefield simulations

Jonathan Wolf,[1] Maureen D. Long,[1] Kuangdai Leng[2,3] and Tarje Nissen-Meyer[2]

[1]*Department of Earth and Planetary Sciences, Yale University, New Haven, CT, USA. E-mail: jonathan.wolf@yale.edu*
[2]*Department of Earth Sciences, University of Oxford, Oxford, UK*
[3]*Rutherford Appleton Laboratory, Harwell Campus, Didcot, UK*

Accepted 2021 August 23. Received 2021 August 18; in original form 2021 March 30

SUMMARY

Observations of seismic anisotropy at the base of the mantle are abundant. Given recent progress in understanding how deformation relates to anisotropy in lowermost mantle minerals at the relevant pressure and temperature conditions, these observations can be used to test specific geodynamic scenarios, and have the potential to reveal patterns of flow at the base of the mantle. For example, several recent studies have sought to reproduce measurements of shear wave splitting due to D$''$ anisotropy using models that invoke specific flow and texture development geometries. A major limitation in such studies, however, is that the forward modelling is nearly always carried out using a ray theoretical framework, and finite-frequency wave propagation effects are not considered. Here we present a series of numerical wave propagation simulation experiments that explore the finite-frequency sensitivity of SKS, SKKS and ScS phases to laterally varying anisotropy at the base of the mantle. We build on previous work that developed forward modelling capabilities for anisotropic lowermost mantle models using the AxiSEM3D spectral element solver, which can handle arbitrary anisotropic geometries. This approach enables us to compute seismograms for relatively short periods (∼4 s) for models that include fully 3-D anisotropy at moderate computational cost. We generate synthetic waveforms for a suite of anisotropic models with increasing complexity. We first test a variety of candidate elastic tensors in laterally homogeneous models to understand how different lowermost mantle elasticity scenarios express themselves in shear wave splitting measurements. We then consider a series of laterally heterogeneous models of increasing complexity, exploring how splitting behaviour varies across the edges of anisotropic blocks and investigating the minimum sizes of anisotropic heterogeneities that can be reliably detected using SKS, SKKS and ScS splitting. Finally, we apply our modelling strategy to a previously published observational study of anisotropy at the base of the mantle beneath Iceland. Our results show that while ray theory is often a suitable approximation for predicting splitting, particularly for SK(K)S phases, full-wave effects on splitting due to lowermost mantle anisotropy can be considerable in some circumstances. Our simulations illuminate some of the challenges inherent in reliably detecting deep mantle anisotropy using body wave phases, and point to new strategies for interpreting SKS, SKKS and ScS waveforms that take full advantage of newly available computational techniques in seismology.

Key words: Numerical modelling; Planetary interiors; Computational seismology; Seismic anisotropy; Wave propagation.

1 INTRODUCTION

The dependence of seismic wave velocities on propagation or polarization direction is known as seismic anisotropy. It has been observed in the crust (e.g., Barruol & Kern 1996; Erdman *et al.* 2013), the upper mantle (e.g., Silver 1996; Chang *et al.* 2014), the mantle transition zone (e.g., Yuan & Beghein 2014; Chang & Ferreira 2019), the lowermost mantle (e.g., Lynner & Long 2014; Long & Lynner 2015; Wolf *et al.* 2019) and the inner core (e.g., Romanowicz *et al.* 2016). Seismic anisotropy yields valuable information on patterns of (past and present) deformation in the Earth, and gives us some of the most direct constraints available about patterns of mantle flow (e.g., Long & Becker 2010). Despite its importance, however, the characterization and interpretation of seismic anisotropy remains challenging and anisotropy is often neglected or simplified (for example, as radial anisotropy) in the construction of seismic models. Some of the major challenges include the limited ray path coverage available for many body wave phases, as well as the (imperfect) assumptions that are made by common measurement methods (for example, when approximating the splitting intensity as a function of backazimuth to resolve upper mantle anisotropy). For the deeper mantle, another challenge is the need to correct for the effects of anisotropy in the shallower parts of the Earth (upper mantle and potentially the crust) in order to isolate the signal from the deeper portions.

The study of seismic anisotropy in the lowermost mantle (here we use this term interchangeably with the D″ layer) is particularly interesting, as there are a number of outstanding unsolved problems related to the structure and dynamics of the core–mantle boundary (CMB) region. Studies of deep mantle anisotropy may potentially shed light on the origin of seismic features such as large low shear velocity provinces (LLSVPs, Reiss *et al.* 2019; Hosseini *et al.* 2019; Davaille & Romanowicz 2020) and Ultra-Low Velocity Zones (ULVZs, Hernlund & Jellinek 2010; Hier-Majumder & Drombosky 2016; Yu & Garnero 2018; Thorne *et al.* 2020, 2021). The characterization of anisotropy at the base of the mantle can potentially illuminate lowermost mantle dynamics, as it has the potential to constrain patterns of mantle flow (e.g., Walker *et al.* 2011; Ford *et al.* 2015). One challenge, however, is that the mineralogy, elasticity and deformation mechanisms associated with lowermost mantle conditions remain imperfectly understood. The main mineral constituents of the lower mantle are likely bridgmanite (Br), calcium silicate perovskite and ferropericlase (Fp); bridgmanite likely undergoes a phase transition to post-perovskite (Ppv) in at least some portions of the lowermost mantle (e.g., Murakami *et al.* 2004; Kaminsky 2017). With the exception of calcium perovskite, these minerals have been inferred to exhibit single crystal anisotropy and thus they may contribute to anisotropy in D″ if deformed via dislocation creep, forming crystallographic preferred orientation (e.g., Nowacki *et al.* 2011). Recently, Creasy *et al.* (2020) established a library of candidate elastic tensors for D″ anisotropy based on viscoplastic self-consistent modelling of texture development for simple deformation geometries for a range of minerals, including polyphase aggregates.

A variety of body wave phases are used to study anisotropy at the base of the mantle, including SK(K)S phases and ScS phases (usually studied in combination with direct *S* phases). The ray paths of these phases are schematically illustrated in Fig. 1. A common observational strategy is to identify pairs of phases that sample the upper mantle in a similar way but propagate differently in the lowermost mantle (such as SKS–SKKS or S-ScS); differences in behaviour between the phases is then attributed to the effects of lowermost mantle structure. Anisotropy is typically measured using the shear wave splitting technique, which accounts for the splitting or birefringence of seismic shear waves when they propagate through an anisotropic medium. Traditionally, shear wave splitting studies estimate the fast direction ϕ, which is the polarization direction of the fast quasi-*S* wave, and the delay time δt, which is the separation in time between the fast and slow quasi-*S* waves. Another observable that is often used in SK(K)S shear wave splitting studies is the splitting intensity (Chevrot 2000), which corresponds to the amplitude ratio between the energy on the transverse component (due to splitting) and the time derivative of the radial component. This observable makes use of the expectation for SK(K)S phases, the conversion from a *P* wave to an *S* wave at the CMB should lead to a wave that is completely radially polarized; deviations from

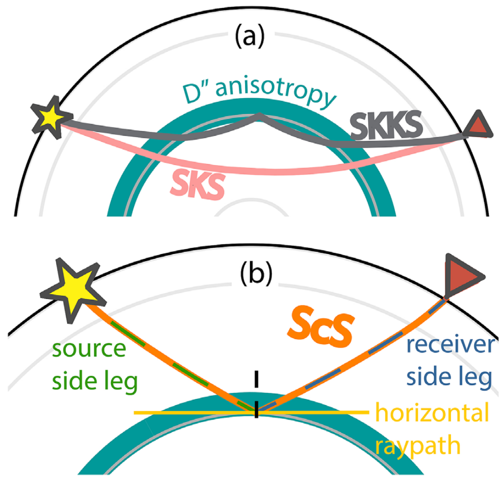

Figure 1. Diagram of ray paths between event (yellow star) and receiver (red triangle). (a) Ray paths of SKS (red) and SKKS (dark grey) for an epicentral distance of 120°. D″ anisotropy is schematically shown in light blue. (b) The ray path of ScS is shown by the solid orange line, with the source side leg marked in green and the receiver side leg in blue (dashed lines). The yellow line represents the approximate ray path of ScS if the phase was travelling horizontally in D″, in the text referred to as the horizontal ray path approximation in the text. Ray path shown for an epicentral distance of 60°.

this indicate the occurrence of shear wave splitting. Several recent studies of lowermost mantle anisotropy using SK(K)S phases have used splitting intensity as a key observation (e.g., Deng *et al.* 2017; Grund & Ritter 2018; Reiss *et al.* 2019; Wolf *et al.* 2019; Lutz *et al.* 2020; Asplet *et al.* 2020).

Observations of anisotropy at the base of the mantle are nearly always made and interpreted in the context of ray theory. Several of the assumptions built into commonly used observational strategies explicitly rely on ray theory (e.g., Wookey *et al.* 2005a; Long 2009). Furthermore, most studies that have sought to explicitly link observations of splitting due to D″ anisotropy to specific mantle flow scenarios via forward modelling have used a ray theoretical framework to compute predicted splitting patterns (e.g., Walker *et al.* 2011; Cottaar *et al.* 2014; Ford *et al.* 2015; Creasy *et al.* 2017; Reiss *et al.* 2019; Wolf *et al.* 2019). Several studies, however, have demonstrated that finite-frequency effects can be important in how anisotropy expresses itself in body waves, both for upper mantle anisotropy (e.g., Favier & Chevrot 2003; Favier *et al.* 2004; Lin *et al.* 2014) and for D″ anisotropy (Nowacki & Wookey 2016; Tesoniero *et al.* 2020). Specifically, Nowacki & Wookey (2016) showed that such effects can be important for ScS phases propagating through realistically complex models for anisotropy at the base of the mantle. Tesoniero *et al.* (2020) showed that finite-frequency effects mostly play a minor role for SK(K)S phases in laterally homogeneous models of lowermost mantle anisotropy, although they can be considerable for some specific geometries.

Several widely used open-source software packages simulate global wave propagation in a framework that is capable of handling anisotropy: SPECFEM3D_GLOBE (Komatitsch & Tromp 2002a, b) is a 3-D spectral-element solver with full anisotropy, AxiSEM (Nissen-Meyer *et al.* 2014) is a 2-D axisymmetric spectral-element solver accommodating axisymmetric anisotropy (van Driel & Nissen-Meyer 2014), and AxiSEM3D (Leng *et al.* 2016, 2019) is a novel 3-D solver that couples a 2-D spectral-element discretization similar to AxiSEM with a pseudospectral Fourier expansion along the third (i.e. non-axisymmetric) dimension for accurate simulations in full 3-D models. Recently, Tesoniero *et al.* (2020) established the ability of AxiSEM3D to handle arbitrary anisotropy, including a benchmark test of AxiSEM3D and SPECFEM3D_GLOBE for a global model that included upper mantle anisotropy (Montagner 2002). The hybrid discretization in AxiSEM3D stems from the observation that wavefields in typical 3-D models maintain a relatively smooth nature along the azimuthal dimension compared to the multi-scale complexity observed in the in-plane propagation direction. This observation holds true for smooth models such as those observed from 3-D global tomography (e.g., Leng *et al.* 2016), but also for much more complex models including interface, topography and bathymetric undulations as well as 3-D salt bodies (Haindl *et al.* 2021). AxiSEM3D exploits this inherent smoothness by expanding the wavefield along the azimuth in a Fourier basis, for instance in a cylindrical coordinate system (s, ϕ, z) as

$$u(s, \phi, z; t) = \sum_{|\alpha| \leq n_u} u^{\alpha}(s, z; t) \exp(\mathrm{i}\alpha\phi), \tag{1}$$

with $u^{\alpha}(s, z; t)$ as the Fourier coefficients of 3-D wavefield $u(s, \phi, z; t)$ within 2-D meridian domain D. Inserting these expressions into the 3-D weak form of the equations of motion yields a system of 2-D weak forms, coupled over the azimuth ϕ. The equivalence between this Ansatz and fully discretized 3-D methods such as SPECFEM3D_GLOBE would be if the Fourier expansion up to n_u would attain the same spatial resolution as within the in-plane direction (s, z). Due to the inherent smoothness of 3-D wavefields, n_u can however be chosen significantly lower while maintaining the same accuracy as the fully discretized approach, and locally amended to the observed wavefield complexity. The accuracy and cost of the method is thus controlled by the number of Fourier coefficients along the azimuth. For more details on the mathematics and implementation behind AxiSEM3D, the reader is referred to Leng *et al.* (2016), Leng *et al.* (2019) and Leng *et al.* (2020). To render this automated and efficient, the concept of wavefield scanning (Leng *et al.* 2019) automatically determines analytical dependencies of wavefield smoothness, as well as trial simulations in order to fix the 2-D map of maximal azimuthal Fourier coefficients. Any desired level of accuracy can be achieved with this convergent method as compared to reference solutions (Leng *et al.* 2016). At sufficient accuracy compared to reference solutions, a speedup between 10 and 1000 is observed (Leng *et al.* 2019; Haindl *et al.* 2021), depending on the smoothness of each application. For a fixed model, the speedup increases with resolution/seismic frequencies, thus enabling simulations for 3-D models up to 1Hz on conventional supercomputing facilities. For shear wave splitting, studies down to 4 s are relevant, rendering this method amenable for such anisotropic studies.

The goal of this work is to examine full-wave effects on shear-wave splitting measurements for laterally heterogeneous models of lowermost mantle anisotropy. For this, we build on the previous study of Tesoniero *et al.* (2020), who examined the finite-frequency sensitivity of SK(K)S waves to laterally homogeneous anisotropy at the base of the mantle. Here we extend this earlier work to consider more realistic models for lowermost mantle anisotropy, including a greater range of elasticity scenarios and increasingly complex models that include lateral variations in anisotropic structure. In doing so, we focus on general patterns for a selection of realistic anisotropy scenarios and elastic tensors rather than comprehensively investigating all possible lowermost mantle elasticity scenarios. We also consider ScS phases, which are commonly used to measure anisotropy at the base of the mantle, in addition to the SK(K)S phases considered by Tesoniero *et al.* (2020). We implement global wavefield simulations in AxiSEM3D for a range of anisotropic models, and compare measurements of commonly used splitting parameters (including fast direction, ϕ, delay time, δt, and splitting intensity, *SI*) from synthetic waveforms with predictions derived from ray theory. We demonstrate that simple lowermost mantle anisotropy scenarios only predict robust shear wave splitting parameters (ϕ, δt) for a relatively narrow range of propagation directions, and this effect depends strongly on the symmetry and other characteristics of the elastic tensor. For ScS waves, we find that it is important to take into account the downgoing and upgoing legs of wave propagation separately when generating ray theoretical predictions of splitting; the commonly used approximation of horizontal propagation is often inaccurate. We show that there are finite-frequency effects when waves sample the boundaries between different anisotropic domains, but the departures from ray theoretical predictions due to such edge effects are generally minor. Our investigations of the minimum size of anisotropic regions (both thickness and lateral dimension) that can be reliably detected reveals that structures larger than roughly 80 km in thickness, and 400 km in lateral extent, are generally detectable at the relevant frequencies, although the details depend on the strength of anisotropy and the characteristics of the elastic tensor. Finally, we show that we can reproduce the findings of ray theory based modelling of a previously published data set that probed splitting due to lowermost mantle anisotropy beneath Iceland when full-wave effects are taken into account.

2 METHODS

2.1 Computation of synthetic seismograms with AxiSEM3D

AxiSEM3D (Leng *et al.* 2016, 2019) can compute 3-D global seismic wave propagation at moderate computational cost, allowing us to calculate seismograms at the relatively short periods (down to 4 s) typically used in shear wave splitting studies. We make use of the anisotropic module implemented in Tesoniero *et al.* (2020) to carry out simulations for a variety of models that include anisotropy in the lowermost mantle. The implementation of Tesoniero *et al.* (2020) allows for models that include anisotropy with arbitrary symmetry. From a user perspective, we must ensure that the mesh is dense enough in regions in which we implement lateral changes between domains with different anisotropy. Additionally, particularly at transitions between different domains, we carefully choose the expansion order of the Fourier series through which AxiSEM3D discretizes structure in the azimuthal direction.

Figs 2 and 3 show examples of typical source and receiver configurations for our numerical experiments. Fig. 2 shows the configuration for a simple, laterally homogeneous model, while Fig. 3 shows a configuration which is designed to understand splitting behaviour across the boundaries between different anisotropic domains. Without loss of generality, we place the receiver at the north pole and place a series of sources at varying azimuths around the receiver, at a distance of 60° for ScS waves and a distance of 120° for SK(K)S waves. (The choice of epicentral distance values is discussed further in Section 2.5). The focal mechanisms are chosen such that the radiation patterns maximize the amplitude of the shear waves under study. For most scenarios we choose moment tensors with M_{tt} as the only non-zero component, although for our purposes, the details of the focal mechanism are not generally important. For ScS waves, the initial polarization of the wave depends on the focal mechanism, and we can change the focal mechanism to investigate a range of

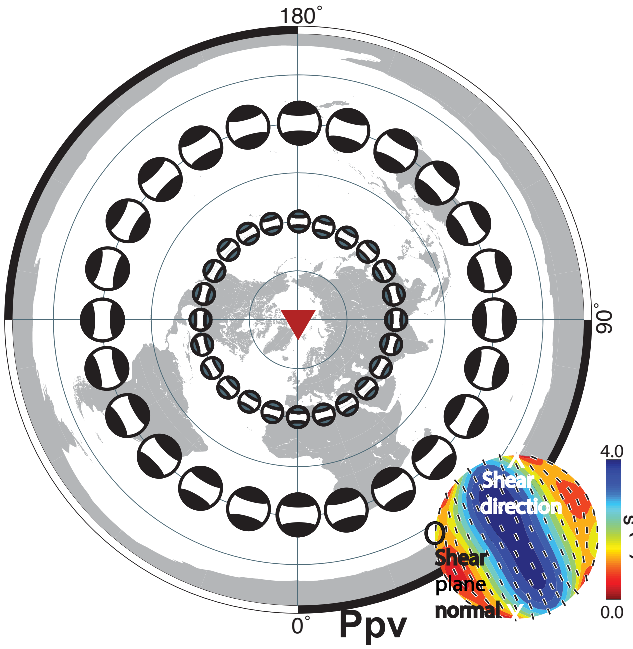

Figure 2. Schematic diagram of a typical source–receiver configuration in our numerical simulations for a simple, laterally homogeneous model. The source–receiver distance is 120° for SK(K)S and 60° for ScS phases. The sources, represented by focal mechanism diagrams, are placed every 5°, more densely than could be visually represented. The only non-zero component of the moment tensors used is M_{tt}; off-diagonal terms are zero. An example Ppv elastic tensor is shown from from above in the inset; black 'O' represents the shear-plane normal and white 'X' represents the shear direction (these are explained in Section 2.2). This example represents simple shear with a vertical shear plane and a horizontal shear direction.

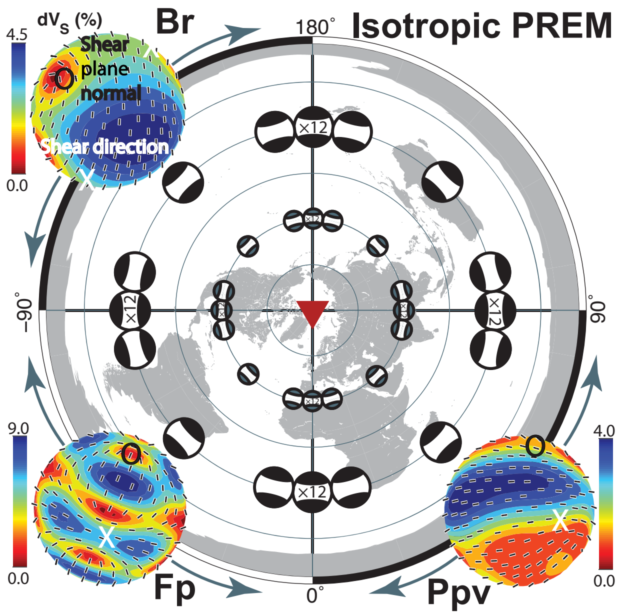

Figure 3. Schematic diagram of the typical source-receiver configuration in a set of numerical simulations, designed to understand splitting behaviour across edges between different domains for a laterally heterogeneous model. The sources are represented by focal mechanism diagrams (as in Fig. 2). The source-receiver distance is 120° for SK(K)S and 60° for ScS phases. The density of simulated earthquakes increases closer to the edge, as indicated by ×12 (=12 earthquakes). Domain edges are chosen to be at longitudes 0°, 90°, 180° and −90°. We implement four domains: Ppv (0–90°), isotropic PREM (90–180°), Br (180−90°) and a Fp (-90°−0°). Elastic tensors are shown from above. A black 'O' represents the shear-plane normal and white 'X' represents the shear direction (these are explained in Section 2.2).

initial polarization directions. For simplicity, we choose the focal mechanism such that the ScS phases are radially polarized in many of our experiments, by rotating the moment tensor appropriately. We mostly use events that are positioned at the surface (depth = 0 km) to avoid any interference from depth phases. In all of our models, we use isotropic PREM (Dziewonski & Anderson 1981) as a background model, and we only modify the structure in the portion of the model that includes anisotropy, as described further later.

For models that include laterally heterogeneous anisotropy, we use more complicated configurations (an example is shown in Fig. 3). The station and event configuration in this example is similar to that in Fig. 2, but we include more densely spaced events at azimuths that are close to the edges between domains (placed at longitudes of 0°, 90°, 180° and –90°). The character of these edges is discussed further in Section 3.2.

2.2 Choice of elastic tensors

One of the goals of our study is to investigate a range of possible mineralogy and elasticity scenarios for lowermost mantle anisotropy. Previous work by Tesoniero *et al.* (2020) focused on elasticity models that were based on single-crystal elastic tensors, mostly derived from *ab initio* calculations (e.g. Wookey *et al.* 2005b). Here we consider a range of more realistic elastic tensors that are derived from the recent work of Creasy *et al.* (2020), who implemented visco-plastic self-consistent texture modelling for simple endmember deformation geometries for different candidate minerals. To do this, Creasy *et al.* (2020) investigated a simple range of endmember deformation geometries including simple shear, pure shear and uniaxial extension. They assumed a set of dominant slip systems (that is, the crystallographic directions for which slip is easiest) based on previous experimental results (see Table S1). For the simple shear case, the macroscopic deformation geometry is defined by the shear plane (specified by its normal vector), or the foliation plane, and the shear direction, or the direction of maximum stretching, as illustrated in Fig. 1 of Creasy *et al.* (2020). For the uniaxial extension case, the macroscopic the deformation geometry is defined by the extension direction. In this work, we focus on a set of elastic tensors that represent bridgmanite (Br), post-perovskite (Ppv) and ferropericlase (Fp) deformed in simple shear from Creasy *et al.* (2020), each with a plausible dominant slip system. Visual representations of the elastic tensors used in this study are shown in Fig. 4, and a description of the tensors and the dominant slip systems is given in Table S1.

We also investigate a few models, discussed further below, that involve simplified versions of the full elastic tensors described in Creasy *et al.* (2020). Specifically, we decompose the Br, Ppv and Fp tensors into higher symmetry approximations (based on the relevant single-crystal symmetries) of the full tensors, in order to investigate the effect of the more complicated tensors (including monoclinic and triclinic components) on splitting patterns. For this, we use the MSAT tool of Walker & Wookey (2012) to decompose the tensors using the tensor decomposition method of Browaeys & Chevrot (2004). Fig. 4 shows the orthorhombic approximations to the Ppv and Br tensors, along with the cubic approximation to the Fp tensor, that are used in these models. Fig. 4 demonstrates that the full Ppv and Br tensors in Creasy *et al.* (2020) are already quite close to orthorhombic in their symmetry; in contrast, Fp has significant lower-symmetry components, and the decomposed Fp tensor is not a particularly good approximation to the full tensor.

2.3 Measurement of splitting parameters

We measure the splitting of synthetic SK(K)S and ScS phases and estimate their uncertainties/errors using a modified version of the SplitRacer code (Reiss & Rümpker 2017). Split-Racer is a graphical user interface implemented in Matlab and is mostly designed to measure the splitting of SK(K)S phases. We modify the code to make it compatible with (1) the distance range used for ScS measurements and (2) the arbitrary initial polarization of ScS waves. Specifically, the modified code can measure the initial polarization of ScS (rather than assuming it to be radial, as is appropriate for SK(K)S) and rotate the horizontal components appropriately before measuring splitting. For this purpose, we calculate the long axis of the particle motion ellipse of ScS phases (using a module already implemented in SplitRacer to detect station misalignment from SK(K)S particle motion). SplitRacer estimates the splitting parameters ϕ and δt using the approach of Silver & Chan (1991) to minimize the transverse component energy (or, in the case of ScS, to minimize the energy along the component orthogonal to the initial polarization direction). The code also measures the splitting intensity (Chevrot 2000), defined as

$$SI = -2\frac{T(t)R'(t)}{|R'(t)|^2} \approx \delta t \sin(2(\alpha - \phi)), \quad (2)$$

where $T(t)$ denotes the transverse component, $R'(t)$ the radial component derivative, α defines the polarization of the incoming wave (equal to 0 for SK(K)S due to the P to S conversion at the CMB), δt the time delay and ϕ the fast polarization direction. Again, for the ScS phases we use the component parallel to the initial polarization direction rather than the radial component. A strength of SplitRacer is the implementation of an automatic multi-window calculation of the splitting parameters, used to statistically evaluate the confidence intervals for the measurements. This procedure minimizes effects from the individual choice of the time window by the user. Furthermore, SplitRacer implements the corrected F-test error formulation for the Silver & Chan (1991) method proposed by Walsh *et al.* (2013). For more details on the technical aspects of the SplitRacer code, we refer to Reiss & Rümpker (2017). Examples of measurements of ϕ, δt and *SI*, with associated errors, for synthetic ScS and SKS waves using the SplitRacer code are shown in Fig. 5. For these, as for all the following measurements, splitting parameters were determined after applying a bandpass filter between 4 and 25 s to the synthetic data.

2.4 Ray-theoretical calculations

For the ray-theoretical calculations, we solve the Christoffel equation using the toolkit christoffel from Jaeken & Cottenier (2016) to predict the splitting parameters ϕ and δt. This approach assumes straight-line ray propagation through the anisotropic layer. The propagation direction was estimated using the TauP package implemented in ObsPy (Beyreuther *et al.* 2010). The splitting intensity (Chevrot 2000) can be estimated from the parameters (ϕ, δt) via eq. (2).

For ScS waves, we try two different approaches to the ray theoretical predictions. In the first, we assume horizontal propagation through D$''$, following previous studies (e.g., Wookey *et al.* 2005a; Nowacki *et al.* 2010; Ford *et al.* 2015). The horizontal ray path approximation is illustrated in Fig. 1(b) by the solid yellow line. In this case, the propagation direction is known, so there is no need to calculate it using TauP before calculating ray-theoretical prediction for the splitting parameters using christoffel. In the second, we consider both legs (Fig. 1b) of the ScS ray path through D$''$ separately and combine them as two different layers. To do this, we calculate the propagation direction for each leg of the ray path separately. With knowledge of the propagation direction, we can use the christoffel toolkit to calculate the splitting parameters ($\phi_{r,i}$, $\delta t_{r,i}$) for the ith leg of the ray path through the anisotropic layer in a ray-centered coordinate system (as opposed to a surface coordinate system, in which the fast polarization direction is measured with respect to the north direction). Due to the CMB reflection, the sign of $\phi_{r,1}$ must be flipped, so that the apparent splitting parameters can be calculated by combining two layers whose splitting is described by ($-\phi_{r,1}$, $\delta t_{r,1}$) and ($\phi_{r,2}$, $\delta t_{r,2}$). Apparent splitting can be calculated with a few different methods; for example those of Silver & Savage (1994) or Bonnin *et al.* (2012), each of which is implemented in MSAT (Walker & Wookey 2012). We use the method of Bonnin *et al.* (2012); to combine both legs of the ScS phase, we generate a first-derivative Gaussian wavelet (period 14 s) and apply the two sets of splitting parameters in sequence by rotating and time-shifting the waveforms appropriately. The best-fitting apparent splitting parameters are then measured by minimizing the second eigenvalue of the covariance matrix (Bonnin *et al.* 2012), for which we use the MSAT (Walker & Wookey 2012) implementation. Finally, we transform the ray-centered splitting parameters to the usual surface coordinate system.

2.5 Choice of distance ranges for ScS and SK(K)S phases

Before implementing simulations for the large range of models considered in this study, we consider the optimal distance ranges for

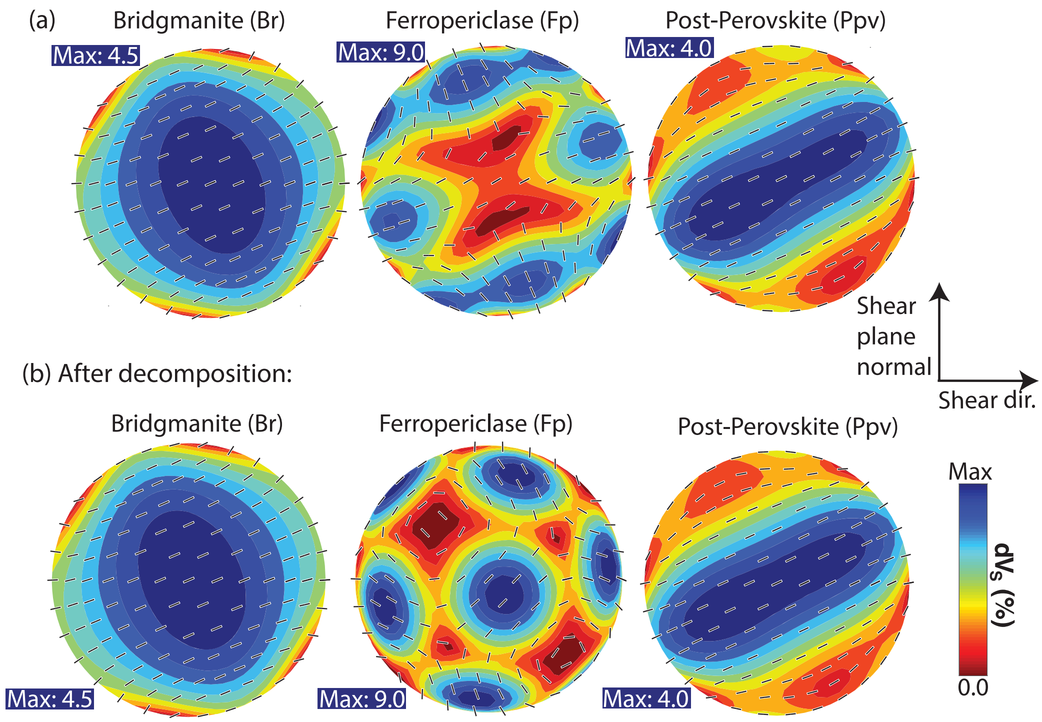

Figure 4. Upper hemisphere representations of the elastic tensors used in this study. The colour scale shows the percentage of *S*-wave anisotropy as a function of direction. The maximum percentage depends on the tensor and is shown at top or bottom left. The small black sticks indicate the fast polarization direction of the *S* wave. Panel (a) shows tensors from Creasy *et al.* (2020) and panel (b) shows the Br, Fp and Ppv tensors after decomposition into higher symmetry approximations (based on the single-crystal symmetries) using the method of Browaeys & Chevrot (2004) as implemented in MSAT (Walker & Wookey 2012). The deformation geometry (shear direction and shear plane normal) is indicated by the arrows at right.

ScS, SKS and SKKS phases for our numerical experiments. We first run a series of simple experiments with a global, homogeneous layer of anisotropy (150 km thick) with an elastic tensor that corresponds to deformed bridgmanite at the base of the mantle. We simulate wave propagation at a variety of epicentral distances for a single azimuth and examine the radial and transverse component synthetics as record sections. For SKS and SKKS, we choose an epicentral distance of 120° for the rest of our numerical experiments, as both phases appear robustly at that distance; transverse component waveforms for other distances are nearly identical. The choice of 120° distance also follows previous work (Tesoniero *et al.* 2020). For ScS phases, the choice of an optimal distance is more complicated. While S–ScS differential splitting measurements are often made for a relatively large swath of epicentral distances (60–85°; Wookey *et al.* 2005a), we find that over some of this distance interval the ScS arrival is contaminated by other phases. Fig. 6 shows a record section aligned on ScS phases; for this case (with a source depth of 0 km), the ScS arrival is only free of contamination at distances 60–72°, and even in this distance range contamination from crustal phases may be significant. This shows that potential contamination of the ScS arrival caused by SP/PS and other phases cannot be neglected in general. While the relative amplitudes of these interfering phases will vary depending on the focal mechanism and focal depth, caution must be applied when analysing ScS phases for anisotropy to avoid contamination from other phases. We choose a distance of 60° for the rest of the simulations presented here in order to avoid such contamination.

3 GLOBAL WAVEFIELD SIMULATIONS: RESULTS AND IMPLICATIONS

3.1 Homogeneous models: effects of mineralogy, tensor symmetry and anisotropy strength

In our first set of numerical experiments, we investigate the dependence of the measured splitting parameters on the direction from which the elastic tensor is sampled. We implemented a suite of simulations using a globally homogeneous anisotropic layer of thickness 150 km at the base of the mantle above the CMB, for anisotropic layers composed of Ppv, Br and Fp. We considered three different sets of models with different strain geometries: horizontal simple shear, vertical simple shear and shear with a vertical shear plane and a horizontal shear direction. As an illustrative example we show results for Ppv for a vertical shear plane and horizontal shear direction in Fig. 7. Results for Br and Fp for the same shear geometry are shown in Figs S1 and S2. Results for Ppv, Br and Fp for the other two shear geometries (horizontal simple shear and vertical simple shear) are shown in Figs S3–S8. We choose the particular example in Fig. 7 (Ppv with a horizontal shear direction and vertical shear plane) because its behaviour is representative and because the delay times for this orientation and layer thickness lead to generally well-constrained splitting parameter estimates. For horizontal simple shear (Figs S6–S8) which is likely the most common strain geometry in the real Earth, a 150-km-layer thickness for Ppv yields generally small delay times and larger error estimates. In the real Earth, the layer thickness may well be larger.

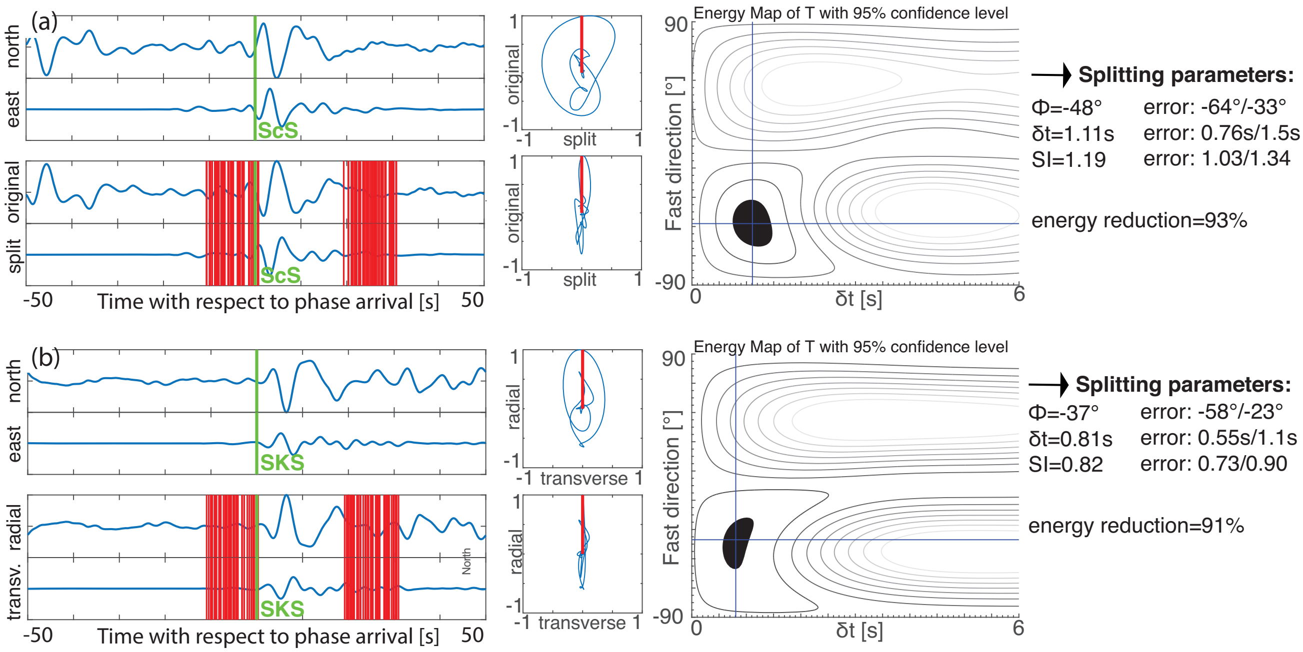

Figure 5. Examples of shear wave splitting measurements on synthetic seismograms. (a) Left-hand panel shows horizontal component seismograms as northeast components (top two traces) and components oriented parallel to the initial polarization ('original') and perpendicular ('split') to it (bottom two traces) for the ScS phase. Green line indicates expected arrival time of the phase. Red lines indicate randomly selected measurement windows. Middle panels show particle motion diagrams (uncorrected, top; corrected for splitting, bottom). Blue line indicates the particle motion, red line indicates the long-axis of the particle motion ellipse (corresponding to the initial polarization). Right-hand panel shows the best-fitting splitting parameters in the ϕ-δt-plane. Black regions indicate 95 per cent confidence regions, calculated using the corrected error formulation for the Silver & Chan (1991) method proposed by Walsh *et al.* (2013). Black crosses indicate the best-fitting splitting parameters. Estimated splitting parameters with error bars, along with estimated energy reduction for the energy minimization method, are shown on the right. (b) Splitting measurements on a synthetic SKS phase. The inital polarization of SKS is controlled by the *P*-to-*S* conversion at the CMB, thus the seismograms are rotated to a radial-transverse reference frame before measuring splitting. The plotting convention is the same as in (a).

Fig. 7 shows the variation in splitting intensity, fast direction (expressed as the difference between ϕ and the backazimuth), and delay time as a function of propagation direction (expressed as the backazimuth) measured from the synthetic seismograms, along with the ray theoretical predictions. We show measurements and predictions for both SK(K)S phases and ScS phases in Fig. 7; for ScS phases, we show ray theoretical predictions both for a horizontal ray path approximation and using the method that explicitly considers the upgoing and downgoing legs of the ScS ray. As illustrated in Fig. 7 and in the supplementary figures, we see that the ray theoretical predictions mostly match full-wave measurements well. At certain backazimuths, slight inaccuracies can be introduced; the ray-theoretical predictions for ϕ appear more robust than for δt and *SI*, irrespective of the seismic phase. For this combination of layer thicknesses and anisotropy strength (the maximum anisotropy strength for the Ppv tensor shown in Fig. 4 is 4 per cent), the predicted delay times are relatively modest (around ∼1 s for both SKS and SKKS) and the error bars on both the ϕ and δt estimates are generally quite large, suggesting that only certain backazimuths would be associated with well-constrained splitting measurements if the traditional measurement methods were used. In contrast, the splitting intensity is well-constrained at all backazimuths. This observation, which is also borne out for other elastic tensor scenarios and strain geometries (Figs S1–S8), may help to explain why the number of well-constrained splitting measurements for the lowermost mantle in real data is so limited: in order to obtain high-quality splitting measurements, the anisotropy must be sampled from an optimal direction, and the combination of anisotropy strength and layer thickness must be appropriate. Specifically, splitting will only be reliably measured at directions for which the splitting is large enough to be detectable (typically greater than ∼0.5 s for realistic noise levels and the relevant periods), but small enough that the assumptions built into the measurement methods (namely, that the delay time is much smaller than the period of the wave) are not violated.

For ScS phases (Figs 7 and S1–S5), we see that the horizontal ray approximation does not generally do a good job of predicting the splitting parameters measured from the full-wave synthetics, while the method that considers both legs of the ray path separately (Fig. 1) mostly does good job of matching the observations. Thus, the horizontal ray path approximation for ScS phases, which has previously been used in many D$''$ anisotropy studies (e.g., Wookey *et al.* 2005a; Ford *et al.* 2015), is found to be an oversimplification.

Predicted splitting patterns for Br and Fp mineralogies (Figs S1 and S2) with the same strain geometry as in Fig. 7 and for models with the other strain geometries (vertical and horizontal simple shear; Figs S3–S8) lead us to generally similar conclusions, although the detailed splitting patterns depend on the elastic tensor used and its orientation. In general, ray theory does a good job of reproducing the full-wave synthetic splitting observations, for both ScS and (especially) for SK(K)S phases; the latter finding is consistent with that of Tesoniero *et al.* (2020) for models based on single-crystal elasticity. One exception is the prediction for Fp for the case of vertical shear (Fig. S4); in this case, ray theory predicts very large delay times for ScS waves, and these delay times are large enough to violate the assumption built in to the measurement

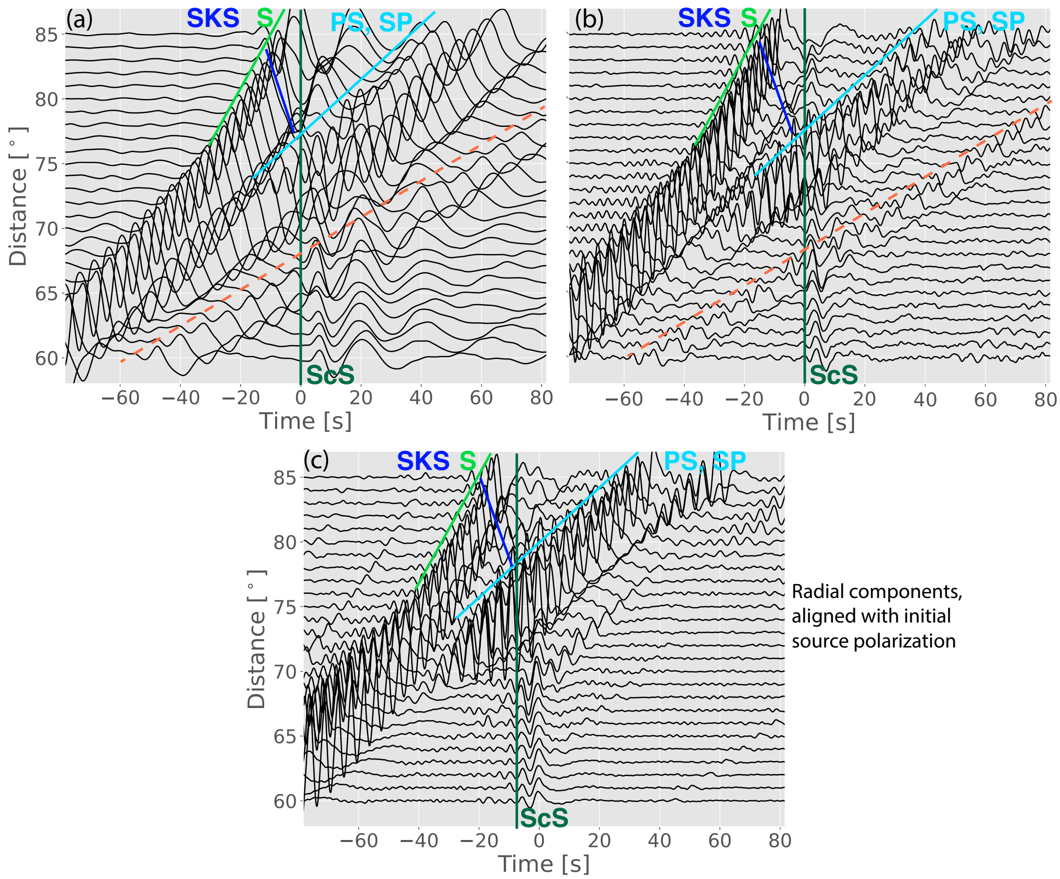

Figure 6. Record section of radial component seismograms aligned on expected ScS arrival. Potentially interfering phases (PS, SP, S and SKS) are labeled. Dashed orange line in (a) and (b) indicates a potentially interfering phase associated with crustal effects; it is not visible in (c). (a) Seismograms for isotropic PREM with attenuation. (b) Seismograms for isotropic PREM without attenuation. (c) Seismograms for a model in which the crust was removed from PREM (velocity value just below the Moho was extended to the surface), without attenuation.

methods that the delay time is much smaller than the dominant period of the wave. (Of course, the assumption of a purely Fp aggregate at the base of the mantle is not realistic for the real Earth, as the lowermost mantle is thought to be ∼15–20 per cent Fp by volume (e.g., Kaminsky 2017), so the anisotropy predicted for this case is unrealistically strong.) For all elastic tensor cases, we find that at many orientations, the predicted splitting parameters (ϕ, δt) have very large error bars, and well-constrained splitting using the traditional measurement method is only obtained over a relatively narrow range of propagation directions.

In order to investigate the effect of the symmetry of the tensor on the splitting predictions, we decompose the Br, Fp and Ppv tensors into higher symmetry approximations (based on the single-crystal symmetries), as discussed in Section 2.2 and shown in Fig. 4(b). This allows us to understand the effect of considering more complicated elasticity models that include lower-symmetry components (triclinic and monoclinic). Results for the original and decomposed tensors for SK(K)S and ScS phases are shown in Fig. 8 (for Ppv) and Fig. S9 for Br. The Fp tensor apparently has substantial lower symmetry components, as shown in Fig. 4(b), so a similarity in splitting parameters between the original and the decomposed tensor would not be expected. We find that because the full Br tensor is nearly orthorhombic even before decomposition, the decomposition has little effect on the splitting parameters (Fig. S9). For Ppv, the general pattern of *SI* as a function of backazimuth is similar for the decomposed and original cases, but the details of the patterns differ. This is true for ScS and SK(K)S (Fig. 8) phases and indicates that higher symmetry approximations based on single-crystal elasticity may not always be suitable for the detailed interpretation of shear wave splitting measurements.

In our final experiment using homogeneous single-layer models, we investigate the minimum thickness of a homogeneous global anisotropic layer required for its detection using shear wave splitting techniques. For this set of model runs, we use the Ppv tensor oriented in an orientation that leads to robust splitting for the chosen propagation direction. We then vary the thickness of the anisotropic layer from 0 to 150 km (starting with increments of 10 km) and measure ϕ, δt and *SI* for the resulting synthetic waveforms (Fig. 9). As would be expected, *SI* increases linearly with layer thickness; we find that the *SI* values are consistently well constrained, with tight error bounds. In contrast, the uncertainties for the traditional methods are large for small layer thickness values (which produce weak splitting) and decrease with layer thickness, implying that the splitting would be too weak to be reliably detected for thin layers. For this particular elasticity scenario (Ppv with an anisotropy strength of 5 per cent), we find that layers with thickness less than ∼80 km cannot be reliably resolved with the traditional splitting parameters. We choose this value because for a layer thickness of ∼80 km or greater the error bars are small enough (uncertainty range of maximum 1 s on δt and 40° on ϕ; see, e.g., Ford *et al.* 2015) that the predicted delay time would likely be considered robust for real data. We acknowledge, however, that the choice of

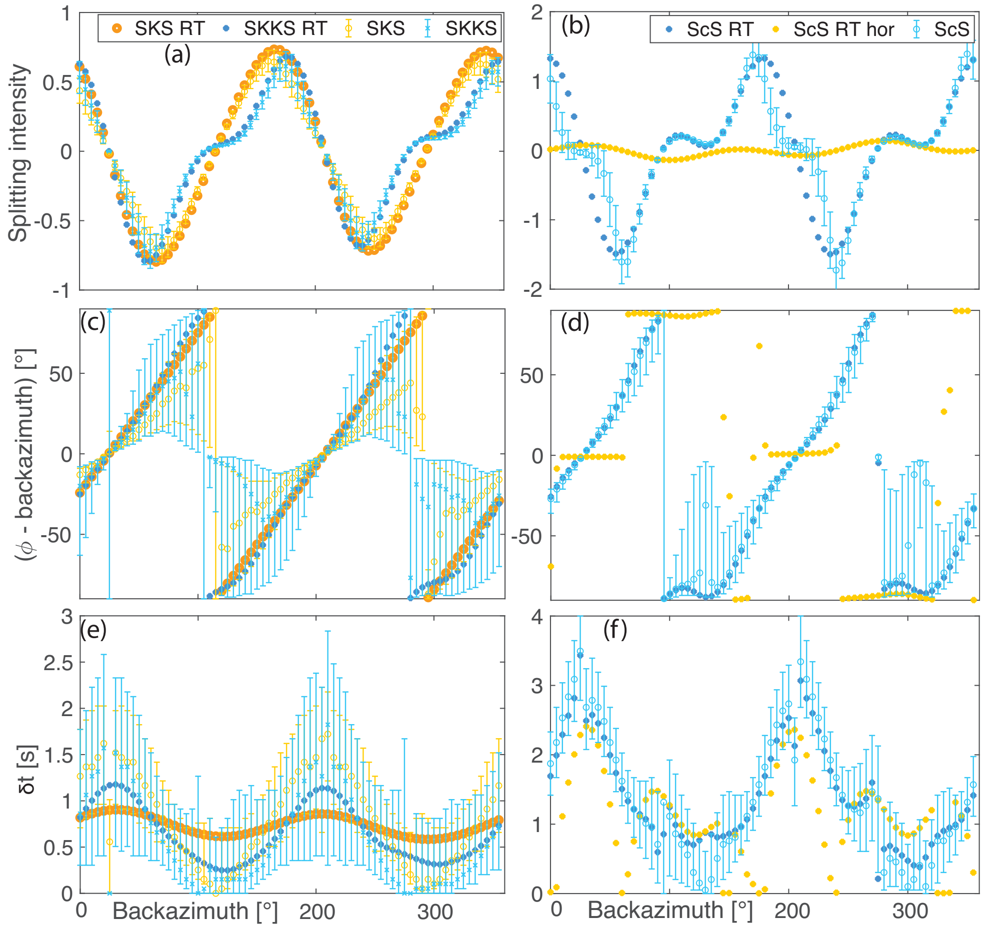

Figure 7. Dependence of splitting parameters on backazimuth for SKS, SKKS and ScS phases for a homogeneous Ppv model (scenario shown in Fig. 2). (a), (c), (e) Measurements of *SI*, (ϕ − *backazimuth*) and δt for SKS (yellow) and SKKS (blue) are compared to their ray-theoretical predictions (RT, see legend). For most backazimuths, the fast polarization direction ϕ and time lag δt show large 95 per cent confidence intervals (bars). (b), (d), (f) Similar to (a), (c) and (e) but here for the ScS phase. Ray-theoretical predictions are shown for the case in which both legs of the ray path through D$''$ are considered separately (RT, see legend) and for the case in which horizontal propagation through D$''$ is assumed (RT hor, see legend).

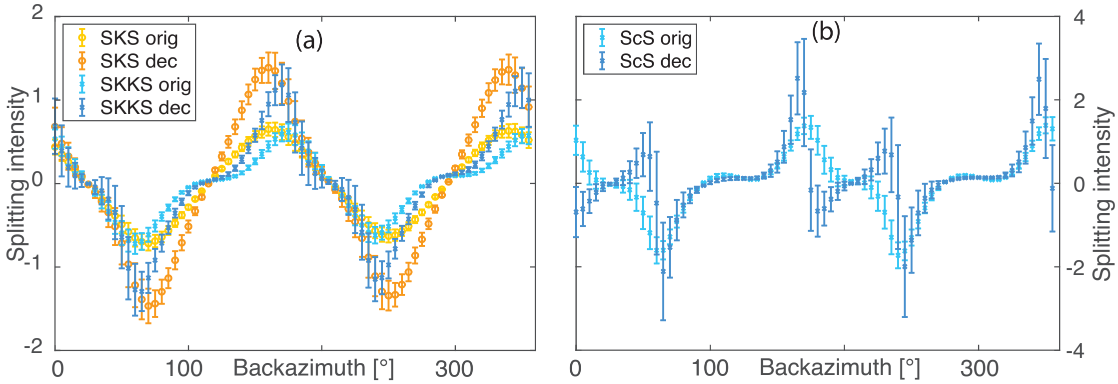

Figure 8. Splitting intensity as a function of backazimuth for homogeneous models of Ppv anisotropy in the lowermost mantle. (a) Splitting intensity for SKS and SKKS for the Ppv tensors from Fig. 4, before (orig, see legend) and after (dec, see legend) decomposition into its orthorombic part. Error bars indicate 95 per cent confidence intervals. (b) Splitting intensity for the ScS phase from the same elasticity scenario as in (a). Plotting conventions as in (a), with details shown in legend.

∼80 km is somewhat subjective and will depend on the details of the elastic tensor. Of course, for the real Earth there will be tradeoffs between the strength of the anisotropy and the thickness of a detectable layer; if anisotropy is stronger, then thinner layers may be detectable and vice versa. Furthermore, these experiments consider noise-free synthetic data; for real, noisy data, the error bars will be larger and the lower limit for detectability may be higher.

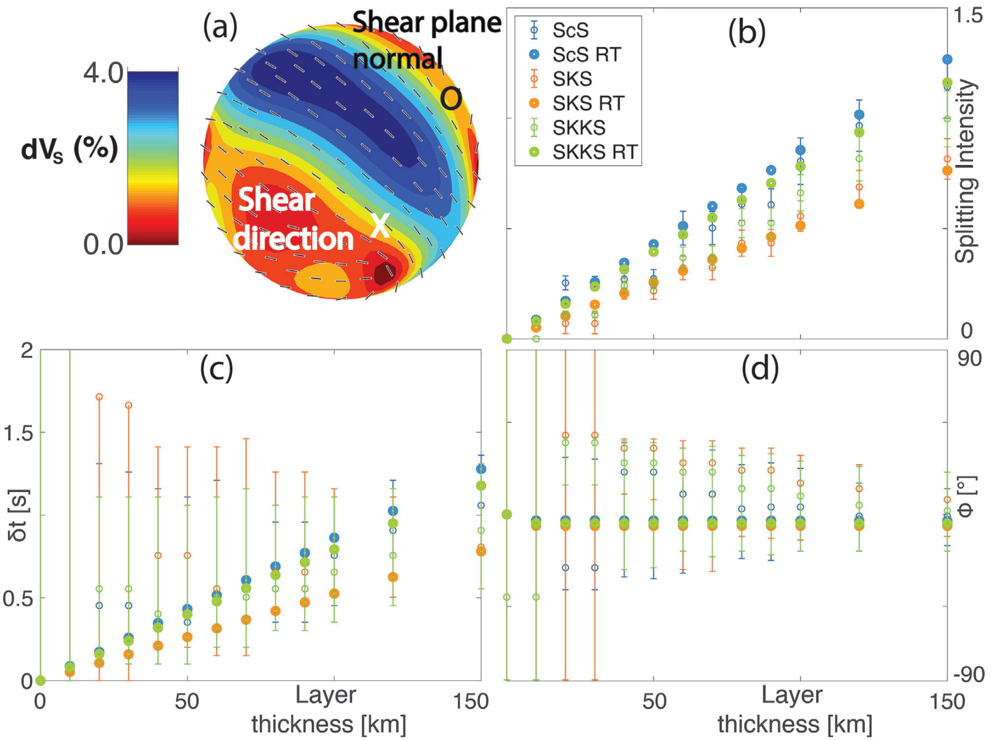

Figure 9. Predicted splitting for a series of homogeneous Ppv models with variable layer thickness. The layer is described by the Ppv elastic tensor shown (looking down from above) in panel (a). The black 'O' represents the shear-plane normal and the white 'X' represents the shear direction. Other panels show ray-theoretical predictions (thick circles, labelled RT in legend) and synthetic measurements for SKS (orange), SKKS (green) and ScS (blue; see legend). (b) Dependence of splitting intensity on layer thickness. (c) Dependence of the time lag δt and (d) the fast polarization direction ϕ on layer thickness. As would be expected, the error estimates (bars) decrease with increasing thickness of the layer.

3.2 Influences of boundaries between different anisotropic domains on splitting parameters

We now investigate the splitting behaviour of waves that sample the boundary between two anisotropic regions with different properties, with the goal of understanding how finite-frequency wave propagation affects measured splitting parameters. In this set of experiments, we are not concerned with understanding how splitting is affected by anisotropic structures of finite horizontal dimensions; rather, we just concentrate on the effects associated with boundaries between different anisotropic domains. The effects of structures with finite dimensions are discussed in Section 3.3. We consider two possible geometric possibilities for anisotropic boundaries: one in which there is a boundary that is parallel to the direction of wave propagation, and the other in which there is a boundary that is perpendicular to the direction of wave propagation.

For the first case, we set up a single global model that includes edges between anisotropic domains, and consider a set of sources (with a receiver at the North Pole) that allow us to efficiently sample these boundaries. Fig. 3 shows the configuration for this model. We consider four domains: isotropic PREM, a Br layer, a Ppv layer and an Fp layer. We choose a layer thickness of 150 km for all models that include an anisotropic layer. For the anisotropic cases, we consider the particular orientations of the tensors that lead to robust splitting for the selected propagation directions as shown in Fig. 3. We situate the edges between anisotropic domains at longitudes of 0°, 90°, 180° and –90°, as shown in Fig. 3. Results for this model configuration are shown in Fig. 10 for SK(K)S and Fig. 11 for ScS phases. Again, we pay particular attention to the splitting behaviour for waves that sample across the boundary, and investigate to what extent ray theoretical predictions are accurate for these phases. Figs 10 and 11 show that the predicted splitting parameters from ray theory and measurements from synthetic waveforms generally agree for all tensors. (Note that for isotropic PREM, we would expect no splitting, which explains the large error bars on the apparent splitting parameters in Figs 10 and 11; in practice, these waveforms would be characterized as robust null, or non-split, measurements.) We find that the ray theoretical fit is slightly worse for ScS phases than for SK(K)S; for example, the ray-theoretical predictions of the fast polarization direction for Fp are outside the 95 per cent confidence interval of the ScS splitting measurements (Fig. 11(d)), while they are within the error bounds for SK(K)S. Furthermore, the ray theory predictions are slightly poorer for the Fp tensor in general. The edges themselves have only a very minor effect on the splitting parameters, and this effect is only observed for waves that propagate at directions that are fractions of a degree away from the edge itself. Further than about 60 km away from the edge, there is no influence on the boundary on the splitting parameters.

For the configuration shown in Fig. 3, we rotate the elastic tensor so that it is sampled from the same direction for each earthquake. Doing this, we make sure that differences in splitting parameters close to the edge can directly be attributed to edge effects and not to the fact that the elastic tensor is sampled from a slightly different direction. A scenario for which the elastic tensor was not rotated is shown in Fig. S10, and the results are similar to those shown in Figs 10 and 11. Due to computational limitations, the edges between the domains in Fig. 3 (and in similar experiments that include laterally variable anisotropy) are not perfectly sharp, but are smoothed over 1°. Given that lateral transitions in structure in the real Earth are unlikely to be perfectly sharp, this approximation

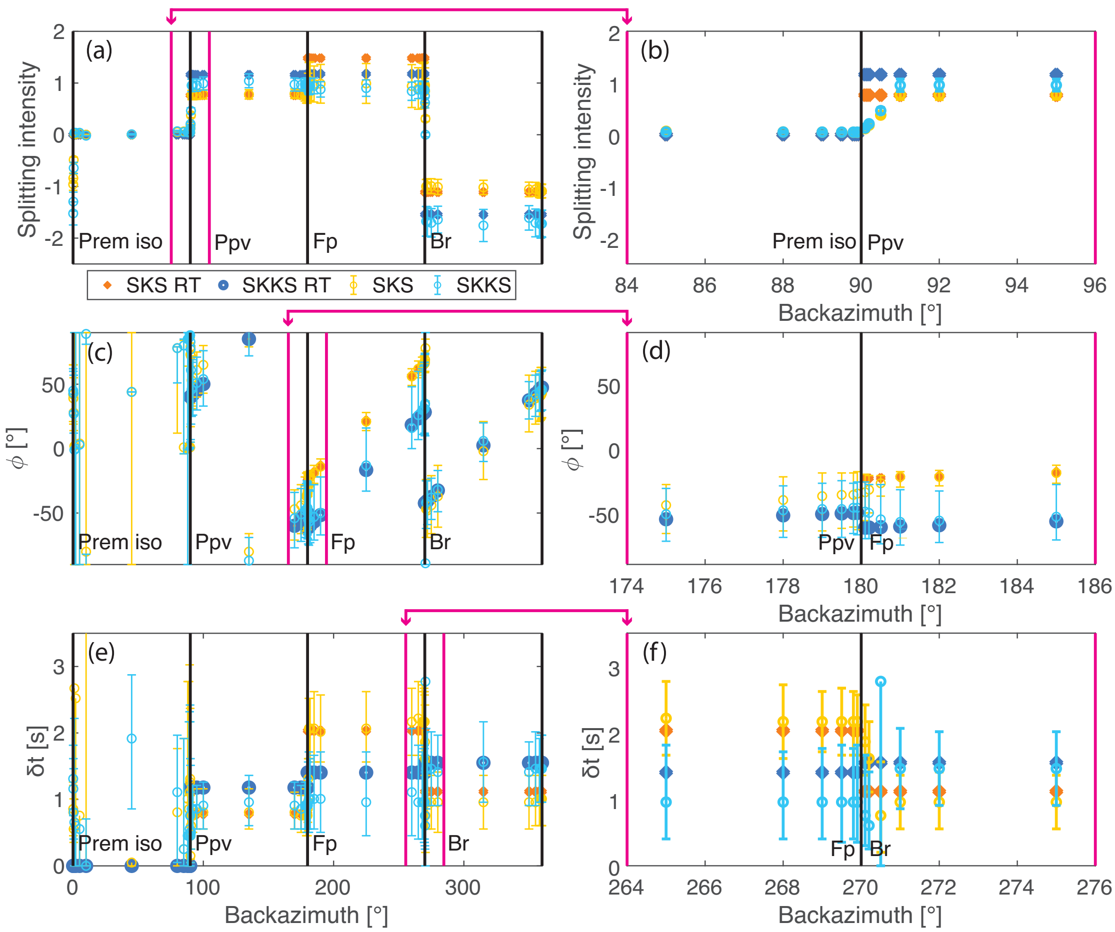

Figure 10. Splitting parameters for SK(K)S phases as a function of backazimuth for the model scenario shown in Fig. 3, which incorporates four distinct anisotropic domains. (a), (c), (e) Measurements of *SI*, ϕ and δt for SKS (yellow) and SKKS (blue) are compared to their ray-theoretical predictions (RT, see legend). Error bars show 95 per cent confidence intervals. Edges between domains are at 0°, 90°, 180° and 270° backazimuth. (b), (d), (f) Same results as in the subfigure to the left, zoomed in on an edge to show detail; as indicated by arrows.

is suitable to evaluate transitions between different domains. We evaluated the effect of using a sharper transition (smoothed over 0.5° instead of 1°) and found that the results were nearly identical (Fig. S11).

We now consider a set of models aimed at investigating the second case, in which the boundary between one anisotropic and one isotropic domain is oriented perpendicular to the wave's propagation direction. To do this, we considered wave propagation through a particular anisotropic model (with a Ppv, Br or Fp layer of thickness 150 km), but introduce a lateral boundary between the anisotropic lower mantle layer and isotropic PREM. We run models with a series of such boundaries that are located progressively farther away from the (ray theoretical) pierce point of the phase in question (SKS, SKKS or ScS) through the top of the anisotropic layer (located 150 km above the CMB). Specifically, we run models for which the boundary is located from 6 km to 310 km from the pierce point (increments of 6, 12, 31, 62, 185 and 310 km). As with our other models, the orientation of the anisotropy is chosen so that robust and high-quality splitting measurements would be expected for the relevant wave propagation direction.

The results of this set of models are shown in Fig. 12. For this experiment geometry, we see that there is more of an effect of the edges on the predicted splitting than for the case in which the boundary is parallel to the direction of wave propagation. For cases in which the boundary is placed relatively close to the pierce point, we see substantial deviations from the ray theoretical predictions (shaded areas in Fig. 12) and the measurements from the synthetic seismograms, with deviations in delay time of up to ∼0.6s and deviations in fast direction of up to ∼30° (depending on the phase type and the mineralogy). When the edge is placed ∼3−5° or more away from the pierce point (corresponding to a distance of ∼185−310 km at the CMB), the differences between ray theory and the full-wave simulations are negligible.

3.3 Anisotropic strips and blobs

We now consider models that incorporate structures of finite lateral dimension, in order to ascertain the (horizontal) length scale of anisotropic structures that can be detected at the base of the mantle. Generally, shear wave splitting is thought to have a high lateral but low vertical resolution (e.g., Savage 1999; Long 2009), at least when it comes to characterizing upper mantle anisotropy with nearly vertically propagating SKS waves. When it comes to characterizing lowermost mantle anisotropy, however, the lateral resolution of SK(K)S and ScS shear wave splitting measurements has not yet been probed in detail from a full-wave perspective. In order to understand how large a region of anisotropy must be in the lowermost mantle in order to cause a clear, robustly measurable effect on the

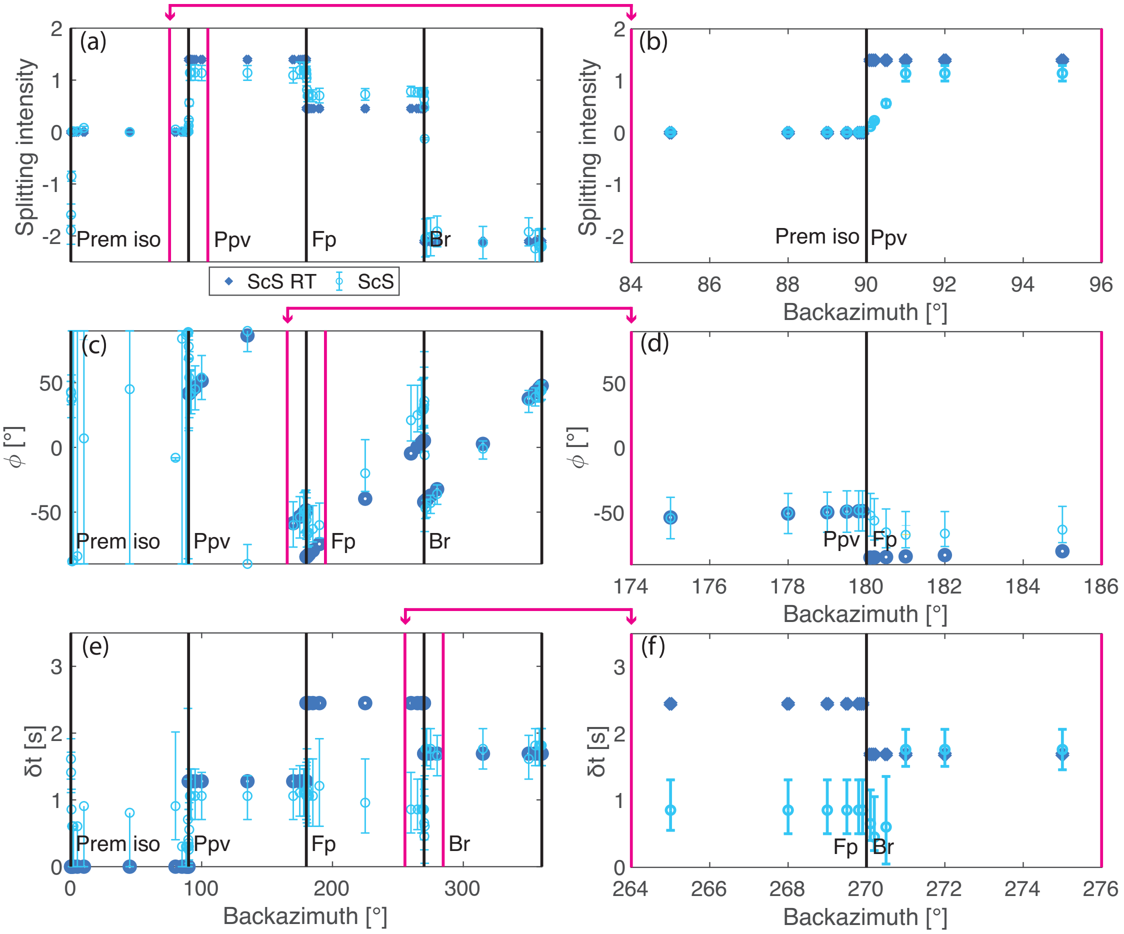

Figure 11. Splitting parameters for the ScS phase as a function of backazimuth for the model scenario shown in Fig. 3, which incorporates four distinct anisotropic domains. (a), (c), (e) Measurements of *SI*, ϕ and δt for SKS (yellow) and SKKS (blue) are compared to their ray-theoretical predictions (RT, see legend). Error bars show 95 per cent confidence intervals. Edges between domains are at 0°, 90°, 180° and 270° backazimuth. (b), (d), (f) Same results as in the subfigure to the left, zoomed in on an edge to show detail; as indicated by arrows.

waveforms, we carry out three different types of numerical experiments. First, we consider structures that are configured as 'strips' of lowermost mantle anisotropy (in a layer of thickness 150 km) that are essentially infinite in one dimension (that is, they wrap around the globe), but have a finite width in the other direction. For our first set of model runs, we implement an anisotropic strip (of finite width) along the equator and adjust our source–receiver configuration so that the pierce points of the SKS, SKKS and ScS phases lie at the equator, with the propagation direction perpendicular to the equator (Fig. 13(a)). In this configuration, the anisotropic strip is oriented orthogonal to the ray path, and we vary the width of the anisotropic strip (from 50 to 700 km; increments of 50 km until 300 km width, then 375, 450, 550 and 700 km width) to find the minimum width that yields an appreciable effect on the waveform, with well-constrained splitting parameters. For our second set of model runs, we still consider a strip of anisotropy, but now the strip is oriented along the prime meridian (with the source-receiver configuration remaining the same), so that the strip is oriented parallel to the ray path (Fig. 13(b)). Again, we vary the strip's width (using the same increments as above) to identify the minimum size needed to reliably detect the anisotropy via shear wave splitting measurements. Finally, in our third set of model runs, we consider anisotropic structures that are finite in both horizontal directions (essentially a 'blob' of anisotropy with a square base area). For this set, we consider two different layer thicknesses (that is, the vertical dimension) of 150 and 250 km, and consider a range of blob sizes (that is, the horizontal dimension) ranging from 50 to 700 km, with the same increments used as for the strip's width.

For this set of models with anisotropic structures of finite lateral extent, we are careful to ensure that our AxiSEM3D runs are set up with sufficient precision to capture the 3-D nature of the structures. We carry out benchmark tests using Fourier expansion orders up to 100 in order to ensure sufficient precision. In order to balance precision against computational cost, we use Fourier expansion orders that led to visually identical results as the results from order 100 for all of the phases considered.

To illustrate our results, we show in Fig. 14 the predictions from the 'strip' and 'blob' tests for SKS phases for a 150-km-thick layer of Ppv. Results for other elastic tensor scenarios (Br and Fp) for SKS are shown in Fig. S12, and results for SKKS and ScS phases (for various elasticity scenarios) are shown in Figs S13 and S14, respectively. The general results from these tests are illustrated well by the results shown in Fig. 14, however. As with our previous tests, we compare our synthetic measurements with the predictions from ray theory, and in Figs 14 and S12–S14 we also compare them with the predictions from equivalent models that have a single, uniform layer of anisotropy of global extent (shown with horizontal bars; the width of the bars is controlled by the size of the error estimates on

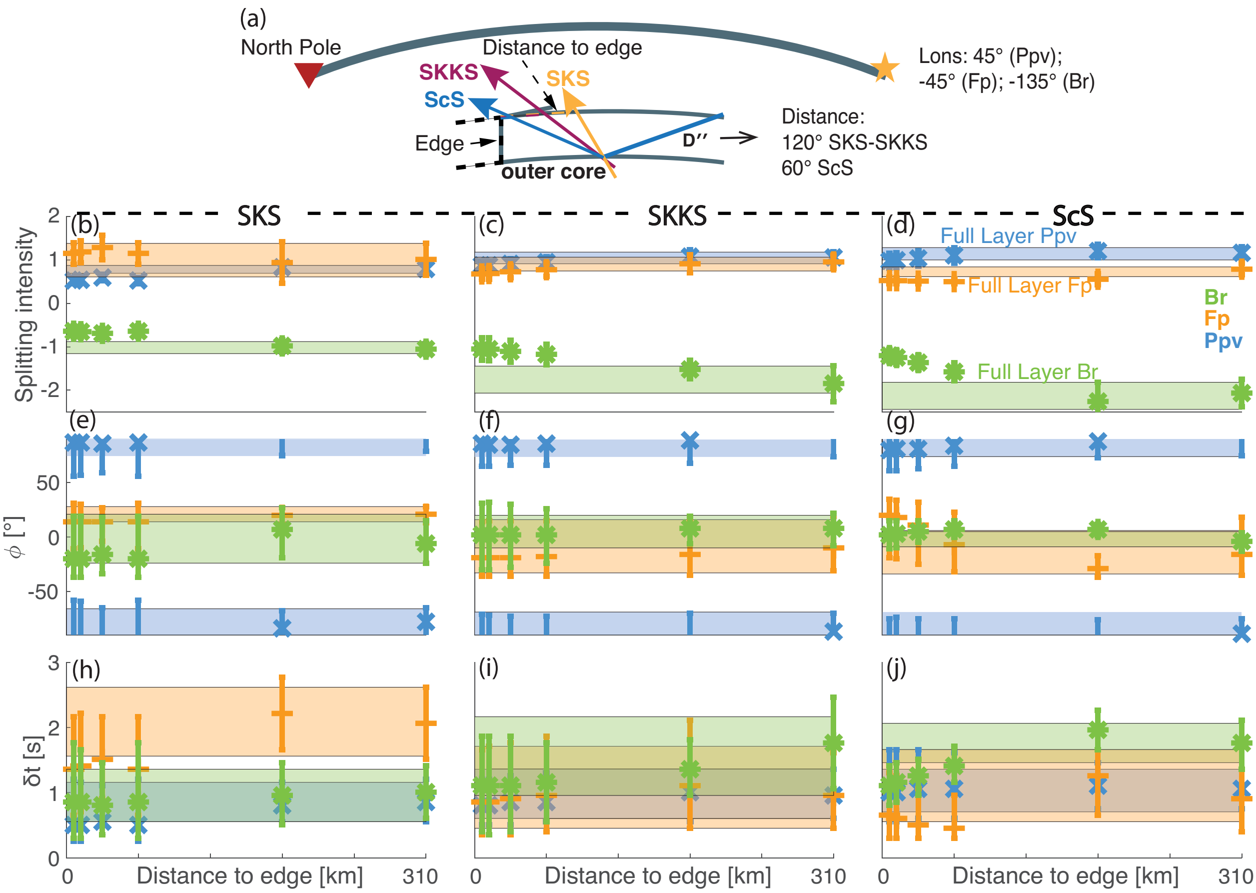

Figure 12. Splitting parameters (*SI*, ϕ and δt) as a function of distance to an edge orthogonal to the ray path plane, as schematically shown in panel (a). The edge is a certain distance (*x*-axis, on panels b–j) away from the upper pierce point of this respective phase at D$''$ on the receiver side. We show splitting results for SKS (b, e, h), SKKS (c, f, i) and ScS (d, g, j) phases. Results for the Br elastic tensor are shown in green, for Fp in orange and for Ppv in blue. Measurements for a full global layer are drawn as shaded areas (indicating the 95 per cent confidence interval) in the colours that match the tensor type.

the splitting parameters estimated from synthetic seismograms for homogeneous models).

Fig. 14 demonstrates that as one would expect, the splitting predicted for an SKS wave sampling an anisotropic strip or blob of finite width tends to converge to the homogeneous global layer case as the size of the anomaly increases, and for anomalies that are ∼400–600 km in size, the synthetic splitting is similar to the global layer case. Again as expected, the synthetic splitting parameters also tend to converge to the ray theoretical predictions as the size of the anomaly increases. We observe very large error bars on the synthetic splitting parameters, particularly for estimates of delay time and fast direction, when the anomaly size is small (and therefore the amount of splitting is also small). Generally, the splitting intensity seems to be more robust and more sensitive to anisotropic structures of any size in contrast to the traditional splitting parameters. Furthermore, it is clear that there are significant differences in synthetic splitting and ray theoretical predictions, particularly for the splitting intensity values, for small anomalies (smaller than ∼400 km in Fig. 14). This suggests that consideration of finite-frequency effects is important when trying to estimate the minimum size of anisotropic bodies that can be detected in D$''$, and we cannot rely on ray theoretical predictions to guide these estimates.

Similar to our findings in Section 3.2 when we investigated edge effects, we find that when the anisotropic strip is oriented orthogonal to the direction of wave propagation, the splitting parameters show larger uncertainties than when the strip is parallel to the propagation direction (Fig. 14). Furthermore, the uncertainties are the largest for the blob models, in which the anisotropic structure is finite in both horizontal dimensions.

In addition to the model shown in Fig. 14, which incorporated a layer thickness of 150 km, we also investigated ‘blob’ models with a thicker anisotropic layer of 250 km, in order to understand whether the minimum horizontal dimension needed to reliably detect anisotropy is different for structures that have a greater vertical extent. A comparison between these two scenarios for SKS phases for the Ppv elastic tensor is shown in Fig. 15, and similar comparisons for SKKS and ScS phases are shown in Supplementary Figs S15 and S16, respectively. (We note that because the Br and Fp elastic tensors have stronger anisotropy than Ppv, the 250 km thick layer model predicted delay times that were large enough to violate the measurement assumptions for the chosen propagation direction; therefore, we only show the 250-km-thick layer test for the Ppv elasticity scenario.) As one would expect, ray theory would predict stronger splitting of SKS phases for the thicker layer case. Interestingly, however, the error bars for splitting parameter estimates made on synthetic SKS phases for the thicker layer case tend to be larger.

Taken together, the model results shown in Figs 14 and 15 as well as Figs S12–S16 allow us to visually assess the scale of anisotropic structures for which we expect to obtain reliable splitting parameters

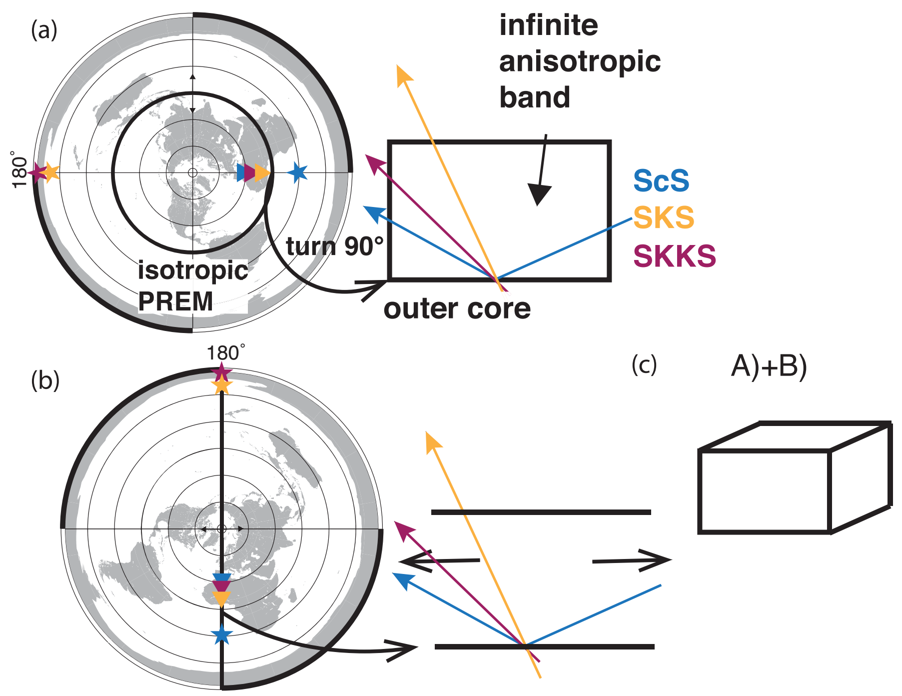

Figure 13. Schematic sketch of the model configurations for the anisotropic 'strip' (A+B) and the anisotropic 'blob' (C) scenarios. The source–receiver configuration is selected such that pierce points of SK(K)S phases through the CMB and the reflection point of the ScS phase are precisely at the equator. Spherical cross-sections of the ray paths for these phases are shown in Fig. 1. Sources are represented as stars and stations as triangles with the colour corresponding to the particular phase. Case (A) Anisotropic band along the equator (orthogonal to the ray path plane); case (B) anisotropic band along the prime meridian (parallel to the ray path plane). The width of these bands is systematically varied. For (C) the model includes an anisotropic 'blob' with a square base area.

for SK(K)S and ScS phases. In general, we find that strips that are oriented parallel to the ray path with a width of less than ∼300 km would not lead to high-quality, well-defined traditional splitting patterns. If splitting intensity measurements are used, somewhat smaller structures might be resolvable, although this will depend on the amount of noise in real data. For strips with edges orthogonal to the ray path, it is unlikely that structures of less than ∼400 km width would be resolvable, particularly with the traditional measurement methods. Similarly, for the blob models, structures on length scales shorter than ∼400 km would be too small to be resolved. Of course, the exact cutoffs for the size of anisotropic structures that would be resolvable in the real Earth would depend on the strength of anisotropy, the layer thickness, and the level of noise in the data, but our models generally suggest that structures smaller than ∼400 km would be unresolvable.

3.4 Realistic Earth scenario—upwelling associated with the Iceland plume

As a final set of models for this study, we carry out a set of numerical experiments that is designed to test whether a previously proposed model for lowermost mantle anisotropy beneath Iceland can reproduce shear wave splitting observations when full wave propagation effects are taken into account. Specifically, Wolf *et al.* (2019) proposed a model for anisotropy at the base of the mantle beneath Iceland that was based on the interpretation of ScS shear wave splitting measurements, which suggest a transition from $V_{SH} > V_{SV}$ anisotropy outside of the plume region to $V_{SV} > V_{SH}$ anisotropy directly beneath the plume. They explained these observations by invoking a cylindrical upwelling at the base of the plume, in a flow scenario similar to that proposed by Yuan & Romanowicz (2017). Wolf *et al.* (2019) tested this conceptual flow model using a range of different elasticity models (based on single-crystal elasticity) for different minerals based on a ray theory approximation. Here, we wish to test whether this conceptual model can match the observations in the context of a global wave propagation simulation, and using the more realistic elastic tensor scenarios proposed by Creasy *et al.* (2020).

In order to test this idea, we implement a simplified version of a cylindrical upwelling geometry, with an approximately circular structure of diameter 800 km centered beneath Iceland (Fig. 16). We choose a layer thickness of 100 km, which yields a synthetic delay time that allows us to obtain well-constrained splitting parameters and avoid violating assumptions made by the splitting measurement method. Within the circular structure, we use elastic tensors for Ppv and Br from Creasy *et al.* (2020) that result from uniaxial extension, rather than simple shear; other assumptions (the dominant slip system(s), the single crystal elasticity, and the amount of strain) are identical to those used in our other simulations. The anisotropy is oriented such that the extension direction is vertical. Outside the circular structure, we assume horizontal simple shear, with the shear direction oriented towards the centre of the upwelling. We considered two different, nearly parallel ScS ray paths (Fig. 16), with one path sampling directly beneath Iceland and one sampling outside of it. While we do not attempt to model the particular ray paths in the Wolf *et al.* (2019) study, this general ray path configuration (with nearly parallel paths that sample within and just outside the region at the base of the plume) is similar. Again, the goal is to understand whether an anisotropic structure of 800 km diameter would find robust expression in the splitting of ScS phases, and could potentially

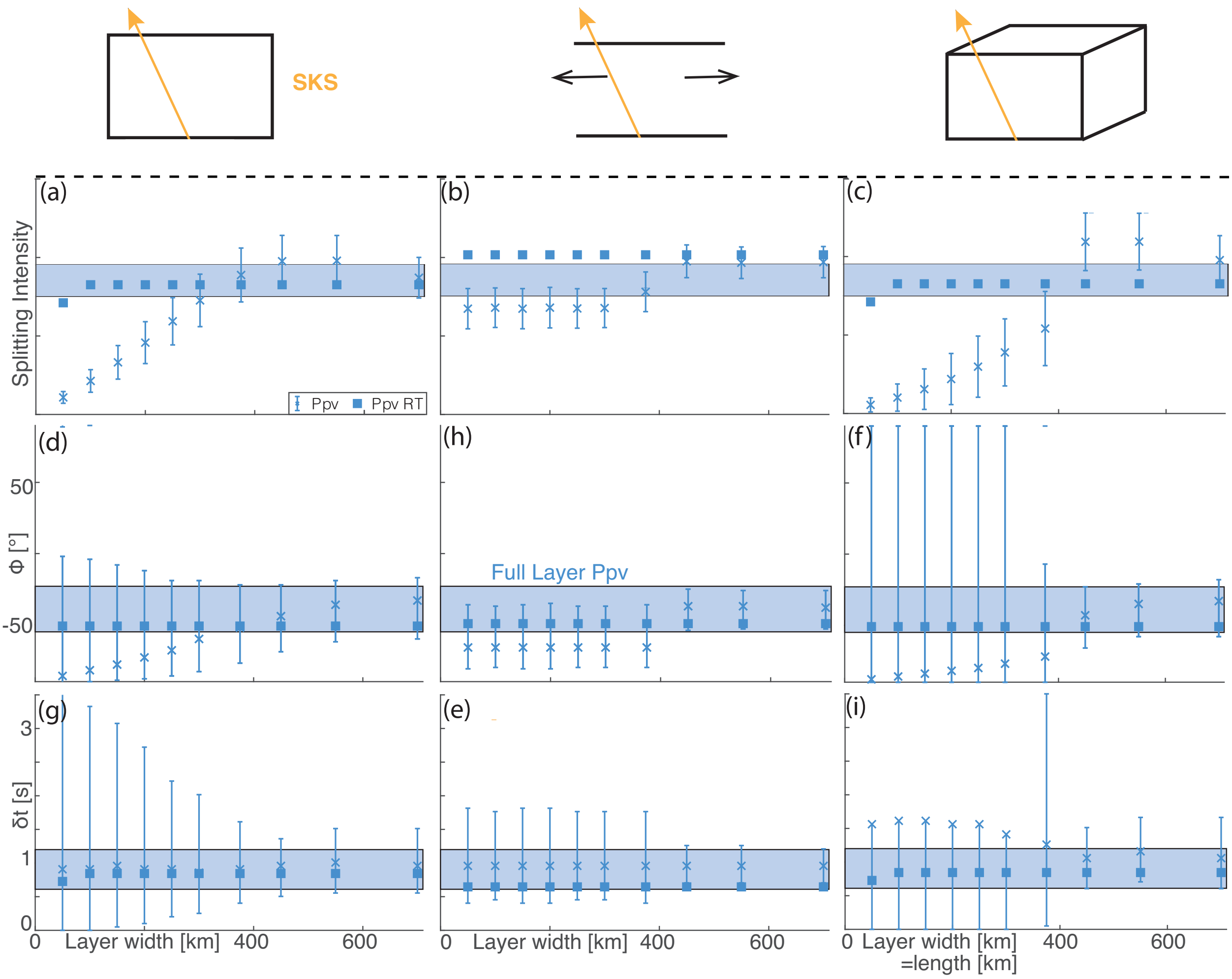

Figure 14. Splitting parameters for the different strip and blob scenarios for the SKS phase, for a Ppv anisotropy model. Panels (a), (d) and (g) show splitting intensity, ϕ and δt for the first scenario; (b), (h) and (e) show these quantities for the second scenario; (c), (f) and (i) show these quantities for the third scenario. Full-wave measurements generally match the ray-theoretical predictions (RT, see legend) only for large dimensions of the anisotropic structures. Error bars for full-wave measurements start to decrease substantially for structures larger than 400 km. Generally, the error bars are larger for the latitudinal band than for the longitudinal band and the largest for the blob scenario. 95 per cent confidence intervals of splitting measurements for a full global layer Ppv are shown as shaded areas.

cause a 90° difference in fast splitting direction, if finite-frequency effects are taken into account. We tested two possible models, one with a Br (Fig. 16) and another with a Ppv (Fig. S17) elastic tensor; the layer thicknesses within and outside the upwelling were approximately 100 km.

Results from these simulations are shown in Figs 16 and S17. We find that for both the Br (Fig. 16) and the Ppv (Fig. S17) scenarios, we are able to reproduce the first-order result from Wolf *et al.* (2019) that ScS phases sampling the lowermost mantle directly beneath the Iceland plume show a fast direction that is consistent with $V_{SV} > V_{SH}$ anisotropy, while ScS phases sampling just outside that region show a fast direction that is consistent with $V_{SH} > V_{SV}$ anisotropy. In other words, the anisotropy scenario that we model, with horizontal simple shear outside the plume and vertical extension (consistent with upwelling) inside of it, would predict a 90° difference in fast splitting direction. This finding is similar to the conclusions of Wolf *et al.* (2019), who carried out ray theoretical modelling of potential upwelling scenarios at the base of the mantle beneath Iceland, and it shows that this conclusion is valid even when finite-frequency wave effects are taken into account. Furthermore, it demonstrates that a relatively localized upwelling of limited spatial extent (Figs 16 and S17) is capable of causing the observed 90° flip in fast splitting directions, even in the context of a realistic global wave propagation simulation, and despite the small size of the presumed upwelling (diameter of 800 km, height of ∼100 km).

4 DISCUSSION

An important question raised by our numerical simulations is that of possible contamination of shear wave splitting measurements by other phase arrivals. Specifically, when trying to determine a convenient distance range for our simulations, we find that the ScS phase is contaminated by other phases for epicentral distances larger than 72° (for a focal depth of 0 km; Fig. 6). For larger focal depths, we must also consider the potential effects of surface-reflected phases (that is, depth phases). Furthermore, even for epicentral distances smaller than 72°, the possibility of contamination from crustal phases cannot be excluded. Contamination from other phases has been shown to

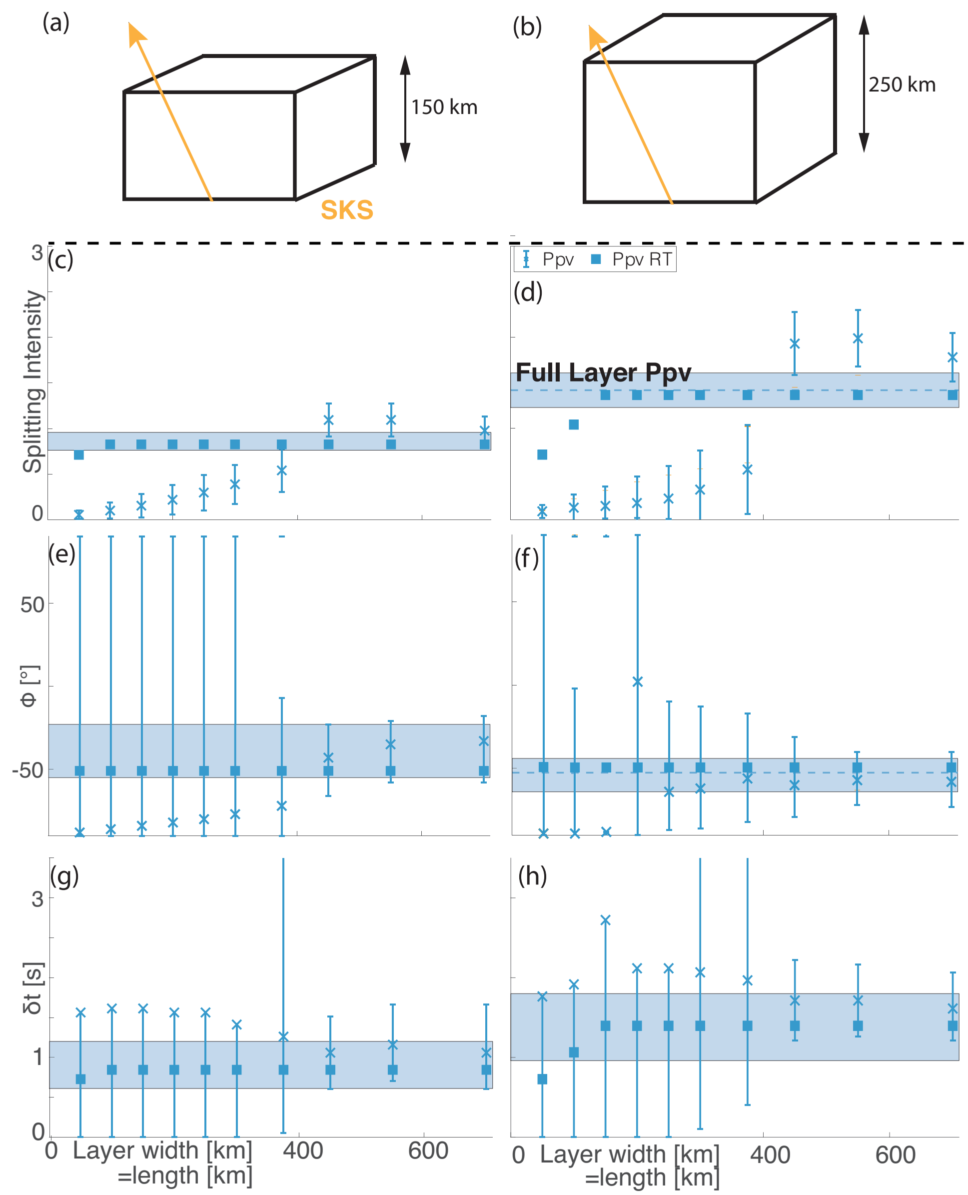

Figure 15. Comparison of two blob scenarios with different thicknesses for SKS phases for the Ppv elastic tensor, as schematically drawn in panels (a) and (b). Splitting intensity, ϕ, and δt for a thickness of 150 km are shown in panels (c), (e) and (g), and for a thickness of 250 km in panels (d), (f) and (h). Layer width (=length) is varied (x-axis). Full-wave measurements match the ray-theoretical predictions (RT, see legend) only for large structures. 95 per cent confidence intervals of splitting measurements for a full global layer of Ppv anisotropy are shown as shaded areas.

potentially mimic splitting for direct S phases, even if no anisotropy is present (e.g., Tono & Fukao 2013), which is why they should be avoided when analysing real data. A straightforward way to do this is to automatically exclude phases that arrive within approximately 10 s of a potential contaminating arrival (as, for example, done by Reiss & Rümpker 2017). If potentially contaminating phases are not preemptively identified, it can be difficult to distinguish their effects on the phase of interest for real data. For example, in the record sections shown in Fig. 6, at a distance of $\sim 75^{\circ}$ ScS and PS phases cannot be discriminated from each other. Our results imply that S-ScS differential splitting Wookey *et al.* (2005a) has to be conducted with great caution for distances larger than 72°, and even for closer distances, the possibility of contamination should be considered. The generation of synthetic seismograms with AxiSEM3D is a useful tool for identifying potentially contaminating phases.

The modelling experiments presented here show that in general, ray theory typically provides a satisfactory approximation to the shear wave splitting behaviour when finite-frequency effects are taken into account, particularly for the simplest, laterally homogeneous models (Figs 7 and S1–S5). This holds for all of the elastic tensor scenarios (Ppv, Br and Fp) that we considered. It is also true for each of the three types of phases examined in this study (SKS, SKKS and ScS), with the SK(K)S synthetics typically yielding splitting parameter estimates that are particularly consistent with ray theoretical predictions. This is true despite the fact that the phases investigated possess a dominant period of $\sim$10s which corresponds to a wavelength of approximately 80 km, which is on the order of magnitude of the layer thickness we consider. Nonetheless, we do not observe substantial effects of trapped energy or diffraction for any of the scenarios we investigated. In cases where we

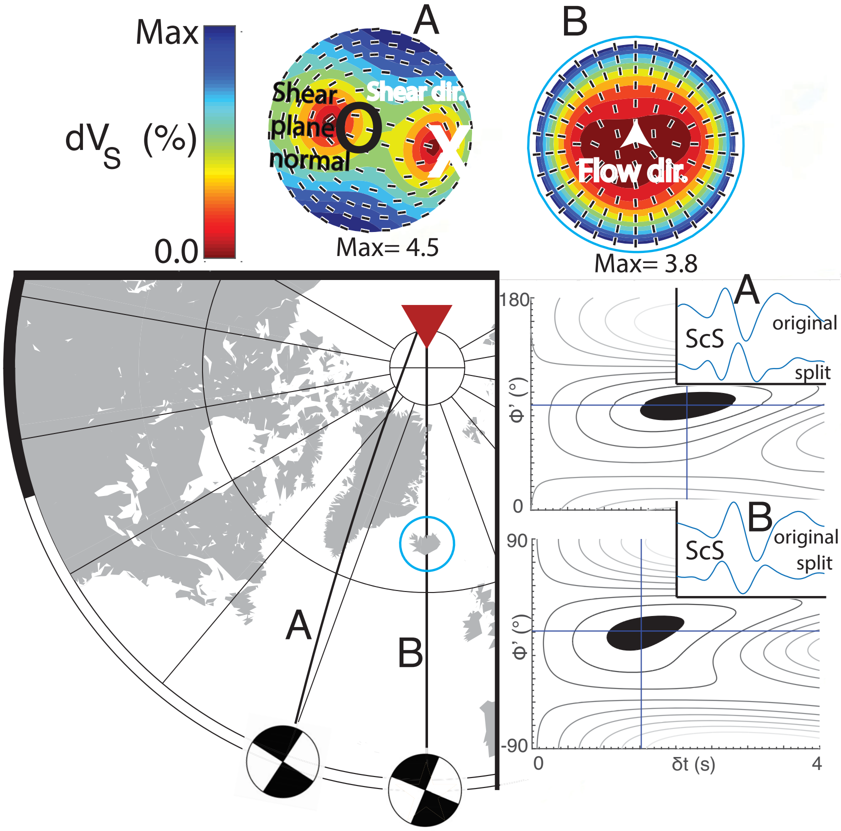

Figure 16. Simulation of a simple seismic anisotropy scenario for the Iceland plume using Br elastic tensors. For the region surrounding Iceland we assume horizontal simple shear; In the upwelling region (blue circle on map) uniaxial extension with a vertical extension direction is used. At the top we show a visual representation of the elastic tensors looking down from above, with a black 'O' representing the shear-plane normal, white 'X' representing the shear direction and a white arrow representing the extension direction (flow direction). At bottom left is a map of the event (focal mechanism), station (red triangle), and ray path configuration. At bottom right are the horizontal component seismograms and splitting parameter estimates. Plotting conventions follow those in Fig. 5. Both scenarios lead to $V_{SV} > V_{SH}$ ($\phi' \approx 0°$) for ray path B (beneath Iceland) and $V_{SH} > V_{SV}$ ($\phi' \approx 90°$) in the surrounding regions (ray path A), consistent with the observations of Wolf *et al.* (2019). A similar plot for a Ppv elastic tensor is shown in Fig. S17.

document significant differences between ray theoretical and full-wave synthetic splitting parameters, it was often the case that the error estimates from the synthetic waveforms were very large, and in practice measurements with such large error bars would likely be discarded. For ScS, we find that it is essential to explicitly consider both the downgoing (before CMB reflection) and upgoing (after CMB reflection) legs of the ScS phase in formulating ray theoretical predictions. While the assumption of a purely horizontal ray path is commonly used in ScS shear wave splitting studies, we have shown that these predictions are substantially less accurate than those that explicitly consider both legs of the ScS ray path.

Another interesting result from our homogeneous, single-layer models is the finding that not only do measured splitting parameters on synthetic SK(K)S and ScS phases vary substantially with azimuth, but the size of the error estimates vary as well and are generally quite large. In fact, well-constrained measurements of the traditional splitting parameters (ϕ, δt) are limited to relatively narrow azimuthal ranges for most of the models we present (e.g. Figs 7, S1 and S5). To highlight one example, for the model shown in Fig. 7 the splitting parameters are highly uncertain for most propagation directions, and particularly for real, noisy data, we would only expect to measure reliable splitting for a few specific azimuths. This may explain the fact that observational studies of D$''$ anisotropy generally yield relatively few clear, well-constrained measurements of D$''$-associated splitting. Furthermore, this observation reflects the tradeoff between anisotropy strength and layer thickness that is inherent in splitting studies; these two combined effects must yield splitting that is strong enough to be detectable (above the limit imposed by error bars; that is the delay time must be significantly larger than the 95 per cent confidence on the δt estimate), but not so strong that the assumptions that are built in to the measurement methods are violated. Specifically teleseismic shear wave splitting measurements rely on δt being much smaller than the wave's dominant period (e.g., Silver & Chan 1991; Chevrot 2000); if δt is large enough to violate this assumption, then the measurements will be inaccurate. For any given elasticity model, this balance will only be achieved over a narrow range of azimuths. In practice, this may mean that even if perfect ray coverage could be achieved for the real Earth, the geometry of anisotropy may not be fully constrained because high-quality measurements cannot be obtained over all azimuths. Our models also show, however, that splitting intensity measurements are typically much better constrained than the traditional (ϕ, δt) parameters, so a focus on high-quality measurements of splitting intensity may help to overcome this limitation.

Our finding that ray theory often provides satisfactory predictions when compared to full-wave simulation also generally holds for more complicated models (across edges and for structures of finite extent), although we document some complications for waves that sample the edges of anisotropic structures. Specifically, we find some modest influence of edges between different anisotropic (and isotropic) domains for some models. We find that across edges, the synthetic splitting parameters do not typically yield unexpected splitting parameters that are unlike what would be expected given the geometry of the anisotropy on either side of the edge. When edges are parallel to the direction of the ray propagation (that is, the source–receiver plane), edge effects are slight (Figs 10 and 11), while they are somewhat larger when the edge is orthogonal to the ray path plane (Fig. 12). Edges orthogonal to the propagation direction can have an effect on the modeled splitting parameters if the ray theoretical path is within $\sim$200−300 km of the edge.

We estimate a minimum thickness of an anisotropic layer that is likely to be detectable at $\sim$80 km (Fig. 9) for plausible elasticity scenarios, although of course there are tradeoffs between the strength of anisotropy and the thickness of the layer, and the actual strength of anisotropy at the base of the mantle is not well known. For anisotropic structures of finite extent such as strips and blobs, we find that structures with widths less than $\sim$300–400 km would be too small to be detectable using traditional splitting measurement methods, so we do not expect to resolve smaller structures in the real Earth using actual data using SK(K)S phases. If splitting intensity measurements are used, then smaller structures may be resolvable, since splitting intensity is a more robust quantity when splitting is weak.

5 CONCLUSIONS

Our modelling experiments show that ray theory is generally suitable to approximate full-wave behaviour of SKS, SKKS and ScS splitting due to lowermost mantle anisotropy. For ScS, ray theoretical predictions must explicitly consider both the upgoing and downgoing legs of the phase in the anisotropic layer. For complex models that include edges between different anisotropic domains and anisotropic structures of finite extent, small to moderate departures from ray theory are predicted. We estimate that a minimum layer thickness of $\sim$80 km is needed to detect anisotropy with commonly used splitting measurement methods, although this will trade off with the strength of anisotropy. Anisotropic structures with length scales of $\sim$300–400 km at the base of the mantle should be theoretically detectable, although in practice with noisy data in the real Earth this limit may be higher. We show that a simple model of a cylindrically symmetric upwelling beneath Iceland that was previously invoked to explain ScS splitting observations, developed in a ray theoretical framework, can plausibly explain the data when finite frequency effects are taken into account.

Finally, and perhaps most importantly, we establish the utility of the anisotropic module of AxiSEM3D to efficiently simulate global wavefield propagation for models that include various elasticity scenarios at the base of the mantle, including heterogeneous structures. We find that ray theoretical predictions of shear wave splitting for simple lowermost mantle anisotropy are generally accurate, validating the philosophy of previous modelling studies based on ray theory (e.g., Nowacki *et al.* 2010; Cottaar *et al.* 2014; Ford *et al.* 2016; Creasy *et al.* 2017; Reiss *et al.* 2019; Wolf *et al.* 2019; Lutz *et al.* 2020). For more complicated anisotropy scenarios, full-wave effects can be significant and may be larger for complex anisotropy in the real Earth. For such cases, our results also point the way towards new modelling approaches for lowermost mantle anisotropy studies that are based on more accurate global wavefield simulations carried out at moderate computational cost. Furthermore, our modelling framework affords the opportunity to realistically simulate the behaviour of multiple body wave phases, allowing for a consideration of possible phase interferences when measuring splitting. Finally, global wavefield simulations have the potential to reveal previously unknown effects of anisotropy on the full seismic wavefield, potentially illuminating new observational strategies.

ACKNOWLEDGEMENTS

This work was funded by Yale University and by the National Science Foundation (USA) via grant EAR-1547499 to MDL. KL and TNM acknowledge support from NERC Grant NE/R012199/1. We gratefully acknowledge the Yale Center for Research Computing for guidance and use of the research computing infrastructure, specifically the Grace cluster. We are grateful to Andrea Tesoniero for advice and discussion on the use of the AxiSEM3D anisotropic module at the beginning of this project. We also thank our colleagues and collaborators for useful discussions, particularly Neala Creasy and Ed Garnero. The Generic Mapping Tools (Wessel & Smith 1998), ObsPy (Beyreuther *et al.* 2010), MSAT (Walker & Wookey 2012) and SplitRacer (Reiss & Rümpker 2017) were used in this research. We thank editor Carl Tape and two anonymous reviewers for constructive comments that helped us to improve the paper.

DATA AVAILABILITY

All synthetic seismograms for this study were computed using AxiSEM3D which is publicly available at https://github.com/kuangdai/AxiSEM-3D.

REFERENCES

Asplet, J., Wookey, J. & Kendall, M., 2020. A potential post-perovskite province in D″ beneath the Eastern Pacific: evidence from new analysis of discrepant SKS–SKKS shear-wave splitting, *Geophys. J. Int.,* **221,** 2075–2090.

Barruol, G. & Kern, H., 1996. Seismic anisotropy and shear-wave splitting in lower-crustal and upper-mantle rocks from the Ivrea Zone: experimental and calculated data, *Phys. Earth planet. Inter.,* **95,** 175–194.

Beyreuther, M., Barsch, R., Krischer, L., Megies, T., Behr, Y. & Wassermann, J., 2010. Obspy: a python toolbox for seismology, *Seismol. Res. Lett.,* **81,** 530–533.

Bonnin, M., Tommasi, A., Hassani, R., Chevrot, S., Wookey, J. & Barruol, G., 2012. Numerical modelling of the upper-mantle anisotropy beneath a migrating strike-slip plate boundary: the San Andreas Fault system, *Geophys. J. Int.,* **191,** 436–458.

Browaeys, J. T. & Chevrot, S., 2004. Decomposition of the elastic tensor and geophysical applications, *Geophys. J. Int.,* **159,** 667–678.

Chang, S.-J. & Ferreira, A. M. G., 2019. Inference on water content in the mantle transition zone near subducted slabs from anisotropy tomography, *Geochem. Geophys. Geosyst.,* **20,** 1189–1201.

Chang, S.-J., Ferreira, A. M., Ritsema, J., van Heijst, H. J. & Woodhouse, J. H., 2014. Global radially anisotropic mantle structure from multiple datasets: A review, current challenges, and outlook, *Tectonophysics,* **617,** 1–19.

Chevrot, S., 2000. Multichannel analysis of shear wave splitting, *J. geophys. Res.,* **105,** 21 579–21 590.

Cottaar, S., Li, M., McNamara, A. K., Romanowicz, B. & Wenk, H.-R., 2014. Synthetic seismic anisotropy models within a slab impinging on the core–mantle boundary, *Geophys. J. Int.,* **199,** 164–177.

Creasy, N., Long, M. D. & Ford, H. A., 2017. Deformation in the lowermost mantle beneath Australia from observations and models of seismic anisotropy, *J. geophys. Res.,* **122,** 5243–5267.

Creasy, N., Miyagi, L. & Long, M. D., 2020. A library of elastic tensors for lowermost mantle seismic anisotropy studies and comparison with seismic observations, *Geochem. Geophys. Geosyst.,* **21,** e2019GC008883.

Davaille, A. & Romanowicz, B., 2020. Deflating the LLSVPs: bundles of mantle thermochemical plumes rather than thick stagnant "piles", *Tectonics,* **39**(10),

Deng, J., Long, M. D., Creasy, N., Wagner, L., Beck, S., Zandt, G., Tavera, H. & Minaya, E., 2017. Lowermost mantle anisotropy near the eastern edge of the Pacific LLSVP: constraints from SKS-SKKS splitting intensity measurements, *Geophys. J. Int.,* **210,** 774–786.

Dziewonski, A. M. & Anderson, D. L., 1981. Preliminary reference Earth model, *Phys. Earth planet. Inter.,* **25,** 297–356.

Erdman, M. E., Hacker, B. R., Zandt, G. & Seward, G., 2013. Seismic anisotropy of the crust: electron-backscatter diffraction measurements from the Basin and Range, *Geophys. J. Int.,* **195,** 1211–1229.

Favier, N. & Chevrot, S., 2003. Sensitivity kernels for shear wave splitting in transverse isotropic media, *Geophys. J. Int.,* **153**(1), 213–228.

Favier, N., Chevrot, S. & Komatitsch, D., 2004. Near-field influence on shear wave splitting and traveltime sensitivity kernels, *Geophys. J. Int.,* **156**(3), 467–482.

Ford, H. A., Long, M. D., He, X. & Lynner, C., 2015. Lowermost mantle flow at the eastern edge of the African Large Low Shear Velocity Province, *Earth planet. Sci. Lett.,* **420,** 12–22.

Ford, H. A., Long, M. D. & Wirth, E. A., 2016. Midlithospheric discontinuities and complex anisotropic layering in the mantle lithosphere beneath the Wyoming and Superior Provinces, *J. geophys. Res.,* **121**(9), 6675–6697.

Grund, M. & Ritter, J. R., 2018. Widespread seismic anisotropy in Earth's lowermost mantle beneath the Atlantic and Siberia, *Geology,* **47,** 123–126.

Haindl, C., Leng, K. & Nissen-Meyer, T., 2021. A 3D complexity-adaptive approach to exploit sparsity in elastic wave propagation, *Geophysics,* **86**(5),

Hernlund, J. & Jellinek, M., 2010. Dynamics and structure of a stirred partially molten ultralow-velocity zone, *Earth planet. Sci. Lett.,* **296,** 1–8.

Hier-Majumder, S. & Drombosky, T. W., 2016. Coupled flow and anisotropy in the ultralow velocity zones, *Earth planet. Sci. Lett.,* **450,** 274–282.

Hosseini, K., Sigloch, K., Tsekhmistrenko, M., Zaheri, A., Nissen-Meyer, T. & Igel, H., 2019. Global mantle structure from multifrequency tomography using P, PP and P-diffracted waves, *Geophys. J. Int.,* **220**(1), 96–141.

Jaeken, J. & Cottenier, S., 2016. Solving the christoffel equation: phase and group velocities, *Comput. Phys. Commun.,* **207,** 445–551.

Kaminsky, F. V., 2017. *Lower-Mantle Mineral Associations,* Springer International Publishing, pp. 23–46.

Komatitsch, D. & Tromp, J., 2002a. Spectral-element simulations of global seismic wave propagation-I. Validation, *Geophys. J. Int.,* **149**(2), 390–412.

Komatitsch, D. & Tromp, J., 2002b. Spectral-element simulations of global seismic wave propagation-II. Three-dimensional models, oceans, rotation and self-gravitation, *Geophys. J. Int.,* **150**(1), 303–318.

Leng, K., Nissen-Meyer, T. & van Driel, M., 2016. Efficient global wave propagation adapted to 3-D structural complexity: a pseudospectral/spectral-element approach, *Geophys. J. Int.,* **207**(3), 1700–1721.

Leng, K., Nissen-Meyer, T., van Driel, M., Hosseini, K. & Al-Attar, D., 2019. AxiSEM3D: broad-band seismic wavefields in 3-D global earth models with undulating discontinuities, *Geophys. J. Int.,* **217**(3), 2125–2146.

Leng, K., Korenaga, J. & Nissen-Meyer, T., 2020. 3-D scattering of elastic waves by small-scale heterogeneities in the Earth's mantle, *Geophys. J. Int.,* **223,** 502–525.

Lin, Y.-P., Zhao, L. & Hung, S.-H., 2014. Full-wave effects on shear wave splitting, *Geophys. Res. Lett.,* **41,** 799–804.

Long, M., 2009. Complex anisotropy in D" beneath the eastern Pacific from SKS–SKKS splitting discrepancies, *Earth planet. Sci. Lett.,* **283,** 181–189.

Long, M. D. & Becker, T., 2010. Mantle dynamics and seismic anisotropy, *Earth planet. Sci. Lett.,* **297,** 341–354.

Long, M. D. & Lynner, C., 2015. Seismic anisotropy in the lowermost mantle near the Perm Anomaly, *Geophys. Res. Lett.,* **42,** 7073–7080.

Lutz, K., Long, M., Creasy, N. & Deng, J., 2020. Seismic anisotropy in the lowermost mantle beneath North America from SKS-SKKS splitting intensity discrepancies, *Phys. Earth planet. Inter.,* **305,** 106504,

Lynner, C. & Long, M. D., 2014. Lowermost mantle anisotropy and deformation along the boundary of the African LLSVP, *Geophys. Res. Lett.,* **41,** 3447–3454.

Montagner, J.-P., 2002. Upper mantle low anisotropy channels below the Pacific Plate, *Earth planet. Sci. Lett.,* **202,** 263–274.

Murakami, M., Hirose, K., Kawamura, K., Sata, N. & Ohishi, Y., 2004. Post-Perovskite phase transition in $MgSiO_3$, *Science,* **304,** 855–858.

Nissen-Meyer, T., van Driel, M., Stähler, S. C., Hosseini, K., Hempel, S., Auer, L., Colombi, A. & Fournier, A., 2014. Axisem: broadband 3-D seismic wavefields in axisymmetric media, *Solid Earth,* **5,** 425–445.

Nowacki, A. & Wookey, J., 2016. The limits of ray theory when measuring shear wave splitting in the lowermost mantle with ScS waves, *Geophys. J. Int.,* **207,** 1573–1583.

Nowacki, A., Wookey, J. & Kendall, J.-M., 2010. Deformation of the lowermost mantle from seismic anisotropy, *Nature,* **467,** 1091–1094.

Nowacki, A., Wookey, J. & Kendall, J.-M., 2011. New advances in using seismic anisotropy, mineral physics and geodynamics to understand deformation in the lowermost mantle, *J. Geodyn.,* **52,** 205–228.

Reiss, M. & Rümpker, G., 2017. SplitRacer: MATLAB Code and GUI for semiautomated analysis and interpretation of teleseismic shear-wave splitting, *Seismol. Res. Lett.,* **88,** 392–409.

Reiss, M. C., Long, M. D. & Creasy, N., 2019. Lowermost mantle anisotropy beneath Africa from differential SKS-SKKS shear-wave splitting, *J. geophys. Res.,* **124**(8), 8540–8564.

Romanowicz, B., Cao, A., Godwal, B., Wenk, R., Ventosa, S. & Jeanloz, R., 2016. Seismic anisotropy in the Earth's innermost inner core: Testing structural models against mineral physics predictions, *Geophys. Res. Lett.,* **43**(1), 93–100.

Savage, M. K., 1999. Seismic anisotropy and mantle deformation: What have we learned from shear wave splitting?, *Rev. Geophys.,* **37,** 65–106.

Silver, P. G., 1996. Seismic anisotropy beneath the continents: probing the depths of geology, *Ann. Rev. Earth planet. Sci.,* **24**(1), 385–432.

Silver, P. G. & Chan, W. W., 1991. Shear wave splitting and subcontinental mantle deformation, *J. geophys. Res.,* **96,** 16 429–16 454.

Silver, P. G. & Savage, M. K., 1994. The interpretation of shear-wave splitting parameters in the presence of two anisotropic layers, *Geophys. J. Int.,* **119**(3), 949–963.

Tesoniero, A., Leng, K., D.Long, M. & Nissen-Meyer, T., 2020. Full wave sensitivity of SK(K)S phases to arbitrary anisotropy in the upper and lower mantle, *Geophys. J. Int.,* **222**(1), 412–435.

Thorne, M. S., Pachhai, S., Leng, K., Wicks, J. K. & Nissen-Meyer, T., 2020. New candidate ultralow-velocity zone locations from highly anomalous SPdKS waveforms, *Minerals,* **10**(3),

Thorne, M. S., Leng, K., Pachhai, S., Rost, S., Wicks, J. & Nissen-Meyer, T., 2021. The most parsimonious ultralow-velocity zone distribution from highly anomalous SPdKS waveforms, *Geochem. Geophys. Geosyst.,* **22,** e2020GC009467,

Tono, Y. & Fukao, Y., 2013. Shear-wave splitting apparently caused by contamination of P-to-S or S-to-P converted waves, *Bull. seism. Soc. Am.,* **103,** 950–957.

van Driel, M. & Nissen-Meyer, T., 2014. Optimized viscoelastic wave propagation for weakly dissipative media, *Geophys. J. Int.,* **199**(2), 1078–1093.

Walker, A. & Wookey, J., 2012. MSAT—a new toolkit for the analysis of elastic and seismic anisotropy, *Comput. Geosci.,* **49,** 81–90.

Walker, A. M., Forte, A. M., Wookey, J., Nowacki, A. & Kendall, J.-M., 2011. Elastic anisotropy of D" predicted from global models of mantle flow, *Geochem. Geophys. Geosyst.,* **12,**

Walsh, E., Arnold, R. & Savage, M. K., 2013. Silver and Chan revisited, *J. geophys. Res.,* **118,** 5500–5515.

Wessel, P. & Smith, W. H. F., 1998. New, improved version of generic mapping tools released, *EOS, Trans. Am. Geophys. Un.,* **79,** 579–579.

Wolf, J., Creasy, N., Pisconti, A., Long, M. D. & Thomas, C., 2019. An investigation of seismic anisotropy in the lowermost mantle beneath Iceland, *Geophys. J. Int.,* **219**(Supplement_1), S152–S166.

Wookey, J., Kendall, J.-M. & Rümpker, G., 2005a. Lowermost mantle anisotropy beneath the north Pacific from differential S-ScS splitting, *Geophys. J. Int.,* **161,** 829–838.

Wookey, J., Stackhouse, S., Kendall, J.-M., Brodholt, J. & Price, G., 2005b. Efficacy of the post-perovskite phase as an explanation for lowermost-mantle seismic properties, *Nature,* **438,** 1004–1007.

Yu, S. & Garnero, E. J., 2018. Ultralow velocity zone locations: a global assessment, *Geochem. Geophys. Geosyst.,* **19**(2), 396–414.

Yuan, K. & Beghein, C., 2014. Three-dimensional variations in Love and Rayleigh wave azimuthal anisotropy for the upper 800 km of the mantle, *J. geophys. Res.,* **119,** 3232–3255.

Yuan, K. & Romanowicz, B., 2017. Seismic evidence for partial melting at the root of major hot spot plumes, *Science,* **357,** 393–397.

SUPPORTING INFORMATION

Supplementary data are available at *GJI* online.

Figure S1: Dependence of splitting parameters on backazimuth for SKS, SKKS and ScS phases for a homogeneous Br model (vertical shear plane with horizontal shear direction). (a), (c), (e): Measurements of *SI*, (ϕ-backazimuth) and δt for SKS (yellow) and SKKS (blue) are compared to their ray-theoretical predictions (RT, see legend). For most backazimuths, the fast polarization direction ϕ and time lag δt show large 95 per cent confidence intervals (bars). (b), (d), (f): Similar to (a), (c) and (e) but here for the ScS phase. Ray-theoretical predictions are shown for the case in which both legs of the ray path through D$''$ are considered separately (RT, see legend) and for the case in which horizontal propagation through D$''$ is assumed (RT hor, see legend).

Figure S2: Like Fig. S1 for a Fp elastic tensor with a vertical shear plane and horizontal shear direction. Plotting conventions are as in Fig. S1.

Figure S3: Like Fig. S1 for a Br elastic tensor with vertical simple shear. Plotting conventions are as in Fig. S1.

Figure S4: Like Fig. S1 for a Fp elastic tensor with vertical simple shear. Plotting conventions are as in Fig. S1.

Figure S5: Like Fig. S1 for a Ppv elastic tensor with vertical simple shear. Plotting conventions are as in Fig. S1.

Figure S6: Like Fig. S1 for a Br elastic tensor with horizontal simple shear. Plotting conventions are as in Fig. S1.

Figure S7: Like Fig. S1 for a Fp elastic tensor with horizontal simple shear. Plotting conventions are as in Fig. S1.

Figure S8: Like Fig. S1 for a Ppv elastic tensor with horizontal simple shear. Plotting conventions are as in Fig. S1.

Figure S9: Splitting intensity as a function of backazimuth for homogeneous models of Ppv anisotropy in the lowermost mantle. (a) Splitting intensity for SKS and SKKS for the Ppv tensor from Fig. 4, before (orig, see legend) and after (dec, see legend) decomposition into its orthorombic part. Error bars indicate 95 per cent confidence intervals. (b) Splitting intensity for the ScS phase from the same elasticity scenario as in (a). Plotting conventions as in (a), with details shown in legend.

Figure S10: Similar to Figs 10 of the main manuscript, but for a scenario in which the elastic tensors are not rotated close to the edges between domains. (a), (b) and (c) show splitting parameters as a function of backazimuth for the model scenario shown in (d). (a), (b), (c): Measurements of *SI*, ϕ and δt for SKS (yellow) and SKKS (blue) are compared to their ray-theoretical predictions (RT, see legend). Error bars show 95 per cent confidence intervals. Edges between domains are at 0°, 90°, 180° and 270° backazimuth. (d) Configuration designed to understand splitting behaviour across edges between different domains for a laterally heterogeneous model. The density of simulated earthquakes increases closer to the edge, as indicated by $\times 12$ (=12 earthquakes). Anisotropic edges are chosen to be at longitudes 0°, 90°, 180° and −90°. We implement four domains: Ppv (0–90°), isotropic PREM (90–180°), Br (180− 90°) and a Fp (−90° to 0°). In contrast to the scenario presented in Figs 3 and 10 of the main text, elastic tensors (shown looking down from above) are not rotated close to the edges. At each edge an orientation of the tensors is chosen that yields well-constrained splitting measurements, visually presented by the upper hemisphere insets of the elastic tensors.

Figure S11: Similar to Figs 10 and 11 of the main text investigating the effect of a denser mesh. Splitting parameters for SK(K)S (upper row) and ScS (lower row) for the scenario shown in Fig. 3 of the main paper. Here, a denser mesh was used (3 elements per wavelength, Courant number 0.5 at 4 s period), plus a denser anisotropy input file (lat, lon). This leads to sharper edges. (a), (b), (c): Measurements of *SI*, ϕ and δt for SKS (yellow) and SKKS (blue) are compared to their ray-theoretical predictions (RT, see legend). Error bars show 95 per cent confidence intervals. Anisotropic edges at longitudes 0°, 90°, 180° and −90°. (d), (e), (f): Like (a), (b), (c) for ScS (blue). with ray-theoretical prediction in yellow.

Figure S12: Similar to Fig. 14 of the main text, but for Br and Fp anisotropy scenarios. Splitting parameters for the different strip and blob scenarios for the SKS phase, for a Br (green) and a Fp (orange) anisotropy model. Panels (a), (d) and (g) show splitting intensity, ϕ and δt for the first scenario (top inset); (b), (h) and (e) show these quantities for the second scenario; (c), (f) and (i) show these quantities for the third scenario. Full-wave measurements generally match the ray-theoretical predictions (RT, see legend) only for large dimensions of the anisotropic structures. Error bars for full-wave measurements start to decrease substantially for structures larger than 400 km. Generally, the error bars are larger for the latitudinal band than for the longitudinal band and the largest for the blob scenario. 95 per cent confidence intervals of splitting measurements for a full global layer Br and Fp are shown as shaded areas.

Figure S13: Like Fig. S12 for elastic tensors Br (green), Fp (orange) and Ppv (blue), for the SKKS phase. Plotting conventions are as in Fig. S12.

Figure S14: Like Fig. S12 for elastic tensors Br (green), Fp (orange) and Ppv (blue), for the ScS phase. Plotting conventions are as in Fig. S12.

Figure S15: Similar to Fig. 15 of the main text, but for SKKS phases. Comparison of two blob scenarios with different thicknesses for SKKS phases for the Ppv elastic tensor, as schematically drawn in panels (a) and (b). Splitting intensity, ϕ, and δt for a thickness of 150 km are shown in panels (c), (e) and (g), and for a thickness of 250 km in panels (d), (f) and (h). Layer width (=length) is varied (*x*-axis). Full-wave measurements match the ray-theoretical predictions (RT, see legend) only for large structures. 95 per cent confidence intervals of splitting measurements for a full global layer of Ppv anisotropy are shown as shaded areas.

Figure S16: Like Fig. S15 for the ScS phase. Plotting conventions are as in Fig. S15.

Figure S17: Simulation of a simple seismic anisotropy scenario for the Iceland plume using Ppv elastic tensors, with the same setup as for Fig. 16 of the main manuscript. For the region surrounding Iceland we assume horizontal simple shear; In the upwelling region (blue circle on map) uniaxial extension with a vertical extension direction is used. At the top we show a visual representation of the elastic tensors looking down from above, with a black 'O' representing the shear-plane normal, white 'X' representing the shear direction and a white arrow representing the extension direction. At bottom left is a map of the event (focal mechanism), station (red triangle), and ray path configuration. At bottom right are the horizontal component seismograms and splitting parameter estimates. Plotting conventions follow those in Fig. 4 of the main manuscript. Both scenarios lead to $V_{SV} > V_{SH}(\phi' \approx 0^\circ)$ for ray path B (beneath Iceland) and $V_{SH} > V_{SV}(\phi' \approx 90^\circ)$ in the surrounding regions (ray path A), consistent with the observations of Wolf *et al*. (2019).

Table S1: Summary of simple shear elastic tensors used in this work from Creasy *et al*. (2020). We show the mineral of interest, the dominant slip system considered, the experimental paper the slip system is based upon and the table in Creasy *et al*. (2020) that contains the individual elastic constants that make up the tensor.

Please note: Oxford University Press is not responsible for the content or functionality of any supporting materials supplied by the authors. Any queries (other than missing material) should be directed to the corresponding author for the paper.